Low SNR microseismic detection using direct *P*-wave arrival polarization

Yusuke Mukuhira*, Oleg V. Poliannikov, Michael C. Fehler, and Hirokazu Moriya

*Corresponding author: Yusuke Mukuhira

−Earth Resources Laboratory, Department of Earth, Atmospheric and Planetary Sciences, Massachusetts Institute of Technology, 77 Massachusetts Avenue Cambridge, Massachusetts 02139-4307, USA: mukuhira@mit.edu

−Current affiliation: Institute of Fluid Science, Tohoku University, 2-1-1 Katahira, Aoba-ku, Sendai, 980-8577: mukuhira@tohoku.ac.jp

Abstract

Detection and analysis of small magnitude events is valuable for better characterization and understanding of reservoirs in addition to developing strategies for mitigating induced seismicity. Three-component receivers, which are now widely used, are commonly deployed in boreholes to provide continuous seismic data amenable to novel and powerful analysis. Using multicomponent continuous records of ground motion, we utilize two principal features of the direct P-wave arrival 1) linearity and 2) polarization in the direction along the ray path to the source region to detect small magnitude events undetectable by conventional methods. We evaluate the linearity of polarization and direction of arrival in the time and frequency domains by introducing the Spectral Matrix analysis method, and combine them into a scalar characteristic function that is thresholded for event detection purposes. We boost the signal-to-noise ratio by stacking characteristic functions obtained at different 3-component receivers along an empirical moveout of a master event known to have occurred in an area of interest. This

allows us to detect smaller events and spatially tie them to a relatively small area around the large event. We apply our method to field data recorded at the Groningen gas field in the Netherlands. Our method detects all catalog events as well as several previously undetected events.

Introduction

The availability of large volumes of continuously recorded data provides an excellent opportunity for multifaceted and innovative seismic analysis. Using continuous data, seismologists can investigate new seismic phenomena, such as slow slip events (e.g., Shelly et al. 2007) or ambient seismic noise (e.g., Shapiro and Campillo 2004). Continuous monitoring and the techniques associated with it, such as template matching methods to detect events, also helps us to understand subsurface processes associated with induced seismicity that accompanies hydraulic fracturing in areas of shale gas development (e.g., Skoumal et al. 2014), and other fields such as Engineered Geothermal Systems (EGS) (e.g., Templeton et al., 2020), and Carbon Capture and Storage (CCS).

Analyzing traditional seismic events originating in a reservoir remains a primary tool for characterizing reservoir processes so having a good algorithm for detecting such events is crucially important. To locate events, we first need to detect their signals within the continuously recorded data. Then we must pick the P- and S- wave arrivals so we can determine hypocenter locations and magnitudes of events. Many earthquake catalogs are populated with events that are detected and picked using conservative methods. However, in the context of monitoring to evaluate the evolution of the reservoir and possible seismic risk, we are typically interested in relatively small events that might not be detected by conventional amplitude based trigger systems. Detecting smaller magnitude events and therefore increasing the total number of detected events is beneficial for a better understanding of the reservoir system, evaluation of the state of stress of the subsurface, and measuring temporal changes in seismic activity for seismic risk management (e.g., Walters et al., 2015).

One of the most well known and widely used earthquake detection methods is the short-time average/long-time average (STA/LTA) (e.g., Allen 1978; Withers et al. 1998) method that is based on the abrupt change of the amplitude as a function of time. Since its invention, a number

of improvements have been proposed (e.g., Akram and Eaton 2016), and other potentially better methods were introduced (Baillard et al. 2014; Langet et al. 2014). Because a lot of these methods depend on amplitude change, they may not perform well on data with a low signal-to-noise ratio (SNR), where the onset of the direct P-wave from a small earthquake is often buried within noise. Template matching, based on cross-correlating a continuous waveform with given template waveforms, is often used in such situations because it is much less sensitive to noise (e.g., Gibbons and Ringdal 2006; Skoumal et al. 2014; Huang and Beroza 2015). Although template matching is robust to noise, it tends to find only events whose waveforms are nearly identical to the template. This introduces a strong bias to the event detection and its performance for detection highly depends on the catalog of template waveforms. There are also hybrid picking methods that combine several amplitude based methods, statistical approaches, and polarization information (e.g. Baillard et al., 2014) with the idea that relying on a consensus between different methods may lead to improved detection algorithms.

In this study, we develop a method specifically for three component (3C) data. Using 3C microseismic data improves the quality of the microseismic data in various ways. Particle motion behavior from 3C components was used to calibrate the orientation of the seismometers (Oye and Ellsworth, 2005) and to rotate the coordinates to enhance the P- and S- wave energy (Gharti et al., 2010). We are particularly interested in detecting aftershocks or foreshocks of known large events but our method has general applicability. It is based on analysis of the particle motion of the direct P-wave, moveout, and direction of arrival information of known (catalog) events. This approach allows us to detect events in a low SNR environment.

Methodology

Concept

When an earthquake occurs, a compressional wave (P-wave) propagates in the heterogeneous earth's crust experiencing scattering and dispersion, and reaches seismometers. One or more cycles of a clear P-wave onset (direct P-wave) are followed by converted and multiply scattered waves that form a P-coda. The direct P-wave may well be the cleanest part of the seismogram and it may contain the most reliable information about the earthquake that produced it. Figure 1 shows examples of 3D particle motion corresponding to different phases of the field-recorded signal from a real earthquake. Particle motion of the noise before the P-wave arrival exhibits random behavior. During the first few cycles of the P-wave arrival, particle motion shows strong linearity along the direction of the P-wave arrival. The arriving S-wave is polarized in the plane perpendicular to the direction of the P-wave polarization. Even some coherent waves coming after the S-wave, that could possibly be converted or reflected waves, show complicated polarization. The S-coda contains a large number of phases that once again lead to apparently random polarization.

The particle motion of the P-wave arrival has two major features: 1) it delineates a linear trajectory, and 2) it is polarized in the direction to the source region along the ray path (Nagano et al., 1989; Shearer, 1999). We utilize both of these features of the P-wave to construct a method for event detection (hereafter referred to as our method but detail will be explained below). These features are common to earthquakes regardless of the source. Linear polarization has often been used in existing event detection/picking methods (Moriya and Niitsuma 1996; Baillard et al. 2014). Polarization information has also been used to detect reflections contained in coda waves (Moriya 2008; Soma et al. 2007). Meersman et al. (2006) used a weighted 3C array method to improve polarization measurements of arrivals in the presence of polarized and correlated background noise. The orientation of the direct P-wave arrival along with the P-S arrival time have been used to locate hypocenters of seismicity using single station recordings (e.g. Frohlich, 1992). However, polarization features have not been used for event detection in

105 low SNR conditions. In this paper, we propose an event detection algorithm and we demonstrate
106 its effectiveness on field data.
107 We first discuss the application of our method to 3-component data from a single station.
108 We construct a characteristic function that combines measures of linearity and the Direction of
109 Arrival (DOA), essentially the angle of incidence, of the ray from the event to the station. We
110 show that this measure is a reliable indicator of the presence of an event in the data. We then
111 show how to stack the characteristic functions derived from data recorded at multiple stations
112 surrounding a master event to detect other, generally smaller, events in the vicinity of the master
113 event.
114
115 Spectral matrix analysis
116 We assume that we have access to continuously recorded 3C digitized data. In the field data
117 we use to illustrate the method, the dominant frequency of seismic events is less than 50 Hz and
118 the sampling frequency of recorded data is 200 Hz. We introduce the spectral matrix (SPM)
119 analysis method to characterize the 3D particle motion in the time-frequency domain. SPM
120 analysis has been used for various purposes such as precise picking of P-wave arrivals (Moriya
121 and Niitsuma 1996), and detection of reflected or polarized seismic waves (Soma et al. 2002;
122 Moriya 2008). The 3D particle motion is represented in the time-frequency domain with the help
123 of the SPM matrix, so we can characterize the polarization by focusing on the frequency band
124 containing a significant portion of the P-wave energy that maximizes the chance to extract direct
125 P-wave arrival features. We expect the SPM matrix analysis to enhance the sensitivity to low
126 SNR data since we evaluate polarity features in a frequency band where the effect of noise is
127 minimal. Our method is independent of source mechanism since polarity features are not
128 dependent on source type but are rather based on the physics of wave propagation from the
129 source to the receiver. Because we use all three available components and consider the

correlation between the different components of the 3-dimensional signal, we expect our method to outperform some conventional methods like STA/LTA and other amplitude-based methods that use single component waveforms.

The spectral matrix is represented as a complex function of time and frequency (Samson, 1977; Moriya and Niitsuma 1996), as follows:

$$S_p(t,f) = \begin{pmatrix} S_{xx}(t,f) & S_{xy}(t,f) & S_{xz}(t,f) \\ S_{yx}(t,f) & S_{yy}(t,f) & S_{yz}(t,f) \\ S_{zx}(t,f) & S_{zy}(t,f) & S_{zz}(t,f) \end{pmatrix} \quad (1)$$

where $S_{ii}(t, f)$ ($i = x, y, z$) are the power spectra; $S_{ij}(t, f)$ ($i, j = x, y, z, i \neq j$) are the cross-spectra estimated with Short Time Fourier transform (STFT) on each moving time window. Each element of the spectral matrix is calculated using a discrete time series windowed around time t, and f denotes frequency that is in practice also discrete and quantized. In what follows we will treat both t and f as continuous variables under the assumption that we can interpolate if necessary. The SPM matrix is calculated continuously in a rolling window centered at time t. Windows may overlap; we find that the method is quite robust to reasonable choices of the parameters of STFT. Below we discuss in more detail the effect of the window on the quality of event detection. Because multiplication by a conjugate in the frequency domain corresponds to cross-correlation in time, the spectral matrix captures linear dependence between the three components in any given window as a variance-covariance matrix. We will use this property of the spectral matrix in the next section.

Evaluation of linearity

We characterize a 3D particle motion using the eigen decomposition of the spectral matrix:

$$S_p(t,f) = [V_1, V_2, V_3] \cdot \begin{bmatrix} \lambda_1 & 0 & 0 \\ 0 & \lambda_2 & 0 \\ 0 & 0 & \lambda_3 \end{bmatrix} \cdot [V_1, V_2, V_3]^T$$

153 (2)

154 Here (λ_i) are the eigenvalues ordered so that $\lambda_1 > \lambda_2 > \lambda_3$, and ($V_k = V_k(t, f)$) are the eigenvectors,
155 where V_k corresponds to the eigenvalue λ_k, for k = 1, 2, 3. We introduce a function C_L to
156 characterize the linearity of the 3-component wave around time t in the frequency band f as
157 follows (Benhama et al., 1988):

158 $$C_L(t,f) = \frac{(\lambda_1 - \lambda_2)^2 + (\lambda_1 - \lambda_3)^2 + (\lambda_2 - \lambda_3)^2}{2(\lambda_1 + \lambda_2 + \lambda_3)^2}$$

159 (3)

160 where $\lambda_i = \lambda_i(t, f)$. The function C_L varies between 0 and 1, and its value indicates the degree of
161 linearity (e.g., C_L = 1: particle motion delineates a rectilinear shape, C_L = 0: there is no linear
162 dependence between the components). It is easy to see that C_L = 1 only when λ_1 is much larger
163 than λ_2 and λ_3. In this case, the particle motion is primarily linear in the direction of V_1; the
164 motion in the other directions indicated by the remaining eigenvectors is negligible. We can
165 evaluate the linearity of particle motion as a function of time and frequency by computing C_L (t,
166 f) for all times and all frequencies, or we can focus on the frequency band that has most of the
167 wave energy, and thus achieve the largest signal-to-noise ratio. By averaging C_L across that
168 frequency band, we obtain a time-function $\overline{C_L}$. Mathematically,

169 $$\overline{C_L}(t) = \frac{1}{n-m}\sum_{i=m}^{n+1} C_L(t, f_i)$$

170 (4)

171 where m and n are the frequency indices corresponding to the physical band we consider.

172

173 Evaluation of DOA inclination

174 We perform the eigen decomposition and extract an eigenvector corresponding to the largest
175 eigenvalue. We define DOA θ as

177 $$\theta(t,f) = tan^{-1}\frac{\left|V_{1_z}(t,f_i)\right|}{\sqrt{\left|V_{1_x}(t,f_i)\right|^2 + \left|V_{1_y}(t,f_i)\right|^2}}$$

176 (5)

178 where V_{1x}, $V_{1y,}$ and V_{1z} are the bases components in a Euclidean coordinate system. When the
179 wave is linearly polarized, the direction of arrival (DOA) as shown in Figure 2 has a simple and
180 intuitive meaning. If the wave is not linearly polarized, defining DOA is more problematic. This
181 vector may not have an obvious geometric interpretation, and will in fact typically vary quite
182 rapidly as a function of time. This can be seen by looking at the particle motion of the noise
183 before the direct P-wave arrival or deep in the S-wave coda, as shown in Figure 1. Even if DOA
184 estimates appear stable when data are noisy it is not clear what, if any, physical significance we
185 can attribute to that. Thus, we will use the DOA estimates only along with estimates of linearity.
186 Note that this definition assumes that the vertical component of the sensor points vertically
187 down. However, the inclination is insensitive to rotations of the receiver in the *xy*-plane. When
188 receivers are installed in a vertical borehole, they may be accidentally rotated, but that will not
189 affect the estimated inclination. Tool orientation will greatly affect any estimate of the azimuth
190 because the azimuth is defined with respect to *x* and *y* axes. Horizontal orientation of the
191 receivers could in principle be calibrated using arrivals from sources with known hypocenters,
192 such as check-shots or previously located earthquakes (Oye and Ellsworth, 2005), so azimuth
193 can be also available. However, in this study we use only the inclination and ignore the azimuth
194 because uncertainty of azimuth is large when there is weak particle motion in the horizontal
195 plane, which is common in our data due to nearly vertical incidence angle at many monitoring
196 situations.
197 Similarly, to $\overline{C_L}$, we define an average DOA inclination, $\bar{\theta}$, by taking the average in the
198 dominant frequency band of the recorded signal:

200 $$\bar{\theta}(t) = tan^{-1}\left[\frac{1}{n-m}\sum_{f=m}^{n+1}\frac{\left|V_{1_z}(t,f_i)\right|}{\sqrt{\left|V_{1_x}(t,f_i)\right|^2+\left|V_{1_y}(t,f_i)\right|^2}}\right]$$

199 (6)

201

202 **Tests using synthetic signals**

203 SNR sensitivity analysis

204 We intend to use our method to detect small events buried in relatively high noise so before
205 applying our method to field data, we first investigate the SNR sensitivity of estimated linearity
206 using a synthetic test. Please also see the performance of this method on a simple synthetic
207 example in the supplemental material (Fig. S1). We prepared 1000 realizations of additive band
208 limited noise and created a synthetic data set by adding sinusoidal P-wave arrivals with different
209 amplitudes to model various SNR conditions: 10, 5, 0, -5, -7, -10 dB. The SNRs are defined as
210 the ratio of the variance of the signal to the variance of the noise. Then, we compute $\overline{C_L}$ in a time
211 window before the P-wave arrival that contains just noise (blue window in Fig. 3a) and a
212 separate time window that contains the sinusoidal P-wave arrival part (red window in Fig. 3a).
213 By repeating the same procedure 1000 times for each noise realization, and plotting histograms
214 of resulting values, we obtain the probability distribution function of $\overline{C_L}$ under different scenarios
215 (just noise or signal+noise) as shown in Figure 3b. If the distributions that correspond to
216 different scenarios do not overlap, then we can distinguish between the scenarios just on the
217 basis of $\overline{C_L}$. When the histograms corresponding to different scenarios overlap, then the amount
218 of overlap indicates the probability of a false alarm based on the use of the amplitude of $\overline{C_L}$ as a
219 detector (flagging an event when there is in fact none). When SNR is relatively high, i.e., greater
220 than 0 dB, the two distributions shown in Figure 3b are clearly separated with little to no
221 apparent overlap, suggesting that our method can detect events almost perfectly. Even when we

222 decrease SNR to -7 dB, the peaks of the distributions are clearly separated, however, the area of
223 overlap increases significantly implying a larger probability of erroneous detection. To
224 summarize, we demonstrate that our method can perform quite well in very noisy environments
225 even for negative SNRs.
226
227 **Application to field data**
228 Groningen, the Netherlands
229 The Groningen gas field is located in the North-East part of the Netherlands. As the biggest
230 gas field in Western Europe, it has provided natural gas since 1963 (Willacy et al. 2018).
231 Historically, the Groningen region had not been seismically active but more recently, a large
232 number of seismic events, including a M3.6 event, have been reported. These seismic events are
233 thought to be caused by compaction of the reservoir associated with gas production (Bourne et al.
234 2014). A dense network of 3C sensors has been deployed around the field in an effort to better
235 monitor and understand this seismicity (Dost et al. 2017; Spetzler and Dost, 2017).
236 We apply our methodology to 4 hours of continuously recorded data starting from
237 00:00:00.315 on 1st November 2016 in a small region within the Groningen field (Fig. 4). The
238 continuous data are sampled at 200 Hz sampling rate. Within this 4-hour period, two large events
239 occurred, and were detected with the conventional method using the amplitude ratio between the
240 events and average noise level, similar to the STA/LTA method, then located and cataloged
241 (Dost et al. 2012). The location threshold was reduced from ~M1.0-M1.5 (van Eck et al. 2004) to
242 ~M0.5 due to network upgrades made since 2014 (Dost et al. 2017; Spetzler and Dost, 2017).
243 The minimum threshold for location varies depending on the location of the event within the
244 Groningen field. From Figure 4 in Dost et al. (2017), the minimum threshold in our study area is
245 M0.5. Phase picks from at least three stations are required for hypocenter determination, (Dost et
246 al., 2017). Thus, we expect that there are more detected but unlocated events than those listed in

247 the KNMI catalog. M0.1 events are listed in the relocated subcatalog in Spetzler and Dost,
248 (2017). During the four-hour time window in our study area, the first catalog event of M1.9
249 occurred at 00:12:28 and another one of M2.2 occurred approximately 45 minutes after the first
250 event. Their hypocenter locations are estimated to be quite close to one another (Fig. 4). We
251 choose 5 stations positioned nearby (named G67, G23, G29, G19, and G24) for our study. Each
252 station in our study consists of a shallow borehole with four 3C seismometers deployed at four
253 levels (50, 100, 150, and 200 m beneath the surface). In total, 20 3C seismometers were used,
254 and they produce 60 traces altogether. These stations are within 4 km from the epicenter of the
255 M1.9 catalog event. Distances of each station from the epicenter of M2.2 event are listed in the
256 caption for Figure 4. Continuous data and the seismic catalog were obtained from the KNMI
257 website (see Data and Resources Section).
258
259 Results
260 To check the applicability of our method, we first apply it to the M1.9 catalog event. As this
261 event has a large magnitude, it is visually apparent and easily detectable by conventional
262 methods, so we use it to check our method. Figure 5a shows normalized 3C waveforms at the 4^{th}
263 level (200 m depth) at station G67. We observe a clear P-wave arrival on the vertical component
264 and a clear S-wave arrival on the horizontal components. Around 1.5 sec after the S-wave arrival,
265 some coherent waves can be seen on all three components. These could be some reflected or
266 converted phase. We compute C_L and θ using a 50 point (0.25 sec) moving time window and one
267 point time shift. Figure 5b shows the time-frequency distribution of C_L estimated from 3
268 component waveforms. We can observe a clear peak around the time of the P-wave arrival over
269 all frequency bands and the peak in C_L lasts less than 0.5 sec. C_L behaves randomly both before
270 the P-wave arrival and soon after the direct P arrival has passed. The average linearity $\overline{C_L}$
271 calculated from the 20~40 Hz frequency band is nearly 1 around the time of the P-wave arrival,

but it also displays high values greater than 0.8 at other times deep in the P-wave and S-wave codas (Fig. 5c). Also we were not able to see any linear polarization feature at the coherent arrival about 1.5 sec after the S wave. This is not at all surprising in light of the fact that a wave travelling in a structure as complicated as the one at Groningen (Dando et al. 2019) generates a large number of conversions and multiples, some of which can be linearly polarized. In the time-frequency distribution of θ shown Figure 5d, we observe a stable part at the P-wave arrival over frequency. We estimate from this figure that the direct P-wave incidence angle is around 60~75°. The DOA estimates become much less stable, and as we argued above, much less meaningful after that. The inclination angle $\bar{\theta}$ averaged over 20~40 Hz, shown in Figure 5e, confirms that the direct P-wave arrives at an incidence angle of 75°, which is consistent with basic geometry and simplified raytracing between the source and receiver. In summary, our method can successfully identify both linearity and inclination of the P-wave arrival from relatively high SNR events recorded in the field. In addition, there is evidence that we could use DOA to detect the arrival of the S-wave. That is we can observe the red zones up to ~40 Hz around the S-wave arrival in DOA distributions of Figure 5d. Linearities of S-wave arrivals are not always high. Averaged DOAs in Figure 5e suggest that DOA of the S-wave arrival is nearly horizontal and perpendicular to the nearly vertical polarization direction of the P-wave. However, examining more details of the S-wave is beyond the scope of this study because we want to exploit the simplicity of the P-wave propagation characteristics. We will examine S-waves in future work.

Now we attempt to detect previously undetected events. Towards that end, we conducted a visual inspection of the same 4 hours of continuous data and detected several events that were not included in the catalog. One of those events occurred 13 seconds after the first (M1.9) catalog event. Figure 6a shows the waveforms at level 4 of station G67 for this event. We applied our method to this event and all computation was performed with the same parameters that we used for the catalog event (Table 1). Our method successfully detects this event.

297 Specifically, we can observe a peak of C_L around the P-wave arrival in Figure 6b. The linearity is
298 high for frequencies greater than about 15 Hz, which is greater than the minimum frequency than
299 for the case of the larger catalog event. As before, $\overline{C_L}$, exhibits peaks not just at the time of the P-
300 arrival but also right after. The subsequent peaks may correspond to SP converted phases
301 generated at one of the interfaces in the subsurface. Another peak can be found around the S-
302 wave arrival time but this peak is not as pronounced as the earlier peaks. S-waves are often found
303 to have elliptical polarization, which will not give rise to high linearity. Turning our attention to
304 the inclination θ, we see in Figure 6d that the yellow color highlight appears at around the P-
305 wave arrival time. The averaged inclination $\bar{\theta}$ indicates that the incident angle of this event is
306 also around 75° just like that of the catalog event examined earlier. While our method is not
307 intended to provide an accurate location, we can hypothesize that this smaller event has
308 originated in the same seismogenic zone where the first catalog event occurred and that the direct
309 P-waves propagated along similar ray-paths that resulted in nearly identical $\bar{\theta}$. In summary, we
310 can detect the linearity and estimate the inclination of arrival of an event that was not detected by
311 a conventional method. Note that we could also use the information of estimated azimuth
312 orientation from P-wave direct arrival particle motion to confirm the seismogenic area, however
313 in this study, we just focus on the inclination as mentioned before.
314
315 Influence of window length
316 Here we analyze the effect of the window length used to calculate the spectral matrix on the
317 performance of $\overline{C_L}$ and $\bar{\theta}$ estimation. We compute $\overline{C_L}$ and $\bar{\theta}$ for different time window lengths of
318 20, 50 100, 150, and 200 sampling points (0.1, 0.25, 0.5, 0.75, and 1 sec, correspondingly) for
319 the same low SNR event that we analyzed before (Fig. 6) and the results are shown in Figure 7.
320 Other parameters remained the same as before (Table 1). Both $\overline{C_L}$ and $\bar{\theta}$ computed with a 20
321 point (0.1 sec) time window have good time resolution and flag the arrival of the direct P-wave

quite precisely. But additionally, we see a lot of peaks $\overline{C_L}$, which could potentially be false alarms. With the increase of the window length, $\overline{C_L}$ and $\bar{\theta}$ become smoother because the longer time window acts as a lowpass filter. The onset of the peak of $\overline{C_L}$ for the P-wave arrival tends to come early for longer time windows. We infer that as soon as polarized particle motion is caught in the time window, the SPM matrix analysis detects the linearity of the wave and $\overline{C_L}$ increases to 1. However, $\overline{C_L}$ will go back down soon after the polarized particle motion is contaminated by random particle motion from the P-wave coda. In summary, shorter time windows increase the time resolution but at the same time, false alarm rates increase. On the contrary, the longer time window can get rid of small spiky peaks that are probably false alarms, but the width of the peak becomes wider causing a loss of time resolution. Here, our focus is not on the precise picking of the P-wave arrival time but on event detection that prefers a more stable measurement to a small time resolution, so we use the 50 point (0.25 sec: red line in Fig. 7) time window for further analysis because that makes $\overline{C_L}$ and $\bar{\theta}$ smooth and reduces the number of false peaks.

Detection of low SNR events

Definition of characteristic function

We showed that our method can extract the two key features of the P-wave arrival, linearity and inclination angle, even from low SNR waveforms. For robust event detection, the two features can be combined to produce a scalar characteristic function (or a score), which can then be thresholded to obtain a final classification. We construct such a characteristic function, which will be the main function used for our detection method, as follows. Assuming that we are interested in smaller events originating in the vicinity of a large master event, we look for directions of arrivals that are similar to that of the master event. A deviation from the DOA of the large event is penalized. This approach is purely ray-geometric and it is therefore robust to

different source mechanisms. We introduce a characteristic function for DOA inclination, C_{DOA}, that penalizes the difference between the measured and reference DOA (θ_0):

$$C_{DOA}(t) = e^{-\frac{1}{2}(\frac{\overline{DOA_{inc}} - DOA_0}{\sigma})^2} \quad (7)$$

where σ is a free parameter that is set heuristically. In subsequent examples, we use σ=10°. This characteristic function decays exponentially especially after difference in DOA becomes more than 10° (Fig. S2 in supplemental material). This function varies from 0 to 1. When the measured and reference DOA (DOA_0) inclinations are the same, C_{DOA} is 1. Recall that we use only the inclination but we could just as easily penalize deviations from the observed azimuths.

The total characteristic function (or a total score), *cf*, combines $\overline{C_L}$ with C_{DOA}, as follows

$$cf(t) = \overline{C_L}(t) \times C_{DOA}(t) \quad (8)$$

We found that using the score *cf* given by Eqn. (8) gives good results for event detection. As $\overline{C_L}$ and C_{DOA} range between 0 and 1, *cf* thus also varies from 0 to 1. Equation (8) should be close to 1 when the following two conditions are satisfied; 1) particle motion shows linearity, 2) measured DOA inclination is similar to reference DOA inclination. By combining linearity with DOA inclination information, we can reject time windows where $\overline{C_L}$ is close to 1 but the wave apparently does not originate from the target seismogenic zone. We rely on the information of V_1 (DOA inclination) only when λ_1 is much larger than λ_2 and λ_3, so $\overline{C_L}$ behaves as a weighting function for C_{DOA}.

Application to low SNR events

We test our characteristic function from Eqn. (8) on the same low SNR event that we used before to check the performance of our linearity and DOA estimators. Figure 8 shows the

calculated functions $\overline{C_L}$, $\overline{DOA_{inc}}$, C_{DOA}, and *cf* using the same parameters as before (Table 1). Here, we use 75° as the reference inclination DOA_0 . The reference inclination matches the estimated inclination of the arrival of the M 1.9 catalog event shown in Figure 5. We observe in Figure 8c that C_{DOA} reaches almost 1 at the time of the P-wave arrival. After the direct P-arrival, C_{DOA} still shows high values but these values will be deemphasized when multiplied by $\overline{C_L}$. C_{DOA} varies more precipitously than $\overline{DOA_{inc}}$ due to the introduction of the exponential cost function from equation. (7). The *cf* in Figure 8d is apparently quieter than both $\overline{C_L}$ and $\overline{DOA_{inc}}$ although we can observe several peaks especially after the P-wave arrival. Using a combination of $\overline{C_L}$ and $\overline{DOA_{inc}}$ drastically enhances the detectability of seismic events from a certain seismogenic region.

Application to continuous field data

Finally, we apply our method to the entire 4 hours of continuous data recorded at 5 monitoring wells having 3 component seismometers at 4 levels. We use the same parameters as before (see Table 1). We use the incident angles of the M1.9 catalog event as the reference DOA inclination DOA_0. Those incident angles are estimated from the deepest seismometer in each monitoring well and used as constant for seismometers in the same well. The reference DOA inclination DOA_0s are 75, 67, 67, 80, and 70 degrees for G67, G23, G29, G19, and G24 respectively. After computing *cf*s for each seismometer, we stack *cf*s shifted according to the moveout shown in Figure 9. This moveout, for all receivers at all depths for all stations, was estimated from the waveforms of the same catalog event by Poliannikov and Fehler, (2018). Stacking moveout-corrected characteristic functions increases the signal-to-noise ratio of *cf*s and thus boosts event detectability. It also further ensures that the detected events likely have originated from the same source region as the master event whose moveout is used for stacking.

Figure 10a shows each *cf*s from all seismometers in the study area. Even before stacking, we can observe coherent peaks across different traces. For some of the seismometers, the noise level in *cf* is not low enough that the peaks indicating P-wave arrivals are pronounced. We also note a number of peaks that are probably false alarms. Figure 10b shows the result of stacking all *cf*s from seismometers in the study area. We can observe that the noise level of *cf* is significantly suppressed down to around 0.2, and that the peaks of the stacked *cf*s are much more visible. We count more than ten clear peaks standing out from the noise in the stacked *cf*. Stacking *cf*s enhances the peaks well, especially the coherent peaks. Indeed, we can detect low SNR events with our proposed method by introducing a proper threshold.

To set the threshold for detection, we first removed 25 % of the smallest and largest data from the stacked *cf*. Then we calculate the median value and the deviation from the median absolute value based on the central limit theorem. Finally, we define the threshold for detection as this median value plus 15 times the median absolute deviation. This process is often used to determine the threshold for detection in the template matching method, and, in some of those cases, the threshold is set as a median value plus 12 times the deviation (Wu et al. 2017), so our detection threshold is relatively conservative.

Figure 11a shows the results of the detection. There are 14 detections including the previously detected catalog events with magnitudes M1.9 and M2.2. Our method detects 6 events shown with triangles in addition to two catalog events (stars) and 6 events detected by visual inspection (diamonds). For each of the detected events, we conducted a visual inspection and confirmed whether the detected result is an event or not. We found that our method could detect 4 additional low SNR events which our visual inspection missed and that 2 detections were false alarms. We found that newly detected low SNR events were so small that clear amplitude/phase changes could not be observed for two most distant stations as shown in Figure 12. The two false alarm events shown with open triangles in Figure 11a arrived just after the M1.9 and 2.2 catalog

events respectively. Therefore, these could be arrivals of some coherent reflection or converted waves, but our visual inspection was unable to confirm that.

Discussion

Using *cf*s stacked for all five boreholes (hereafter referred as cf_{all}), we can detect four additional low SNR events (Table 2). As waveforms of two of them show (Fig. 12), the appearance of P-wave can be observed only at the 3 monitoring stations (G67, G23, and G29) that are nearest to the estimated source region. So, we also tested stacking the *cf*s from different subsets of stations and investigated the performance of the resulting detection algorithm. We calculate the stacked *cf* for the two and three monitoring wells nearest the source region, and also define the thresholds with the same manner to the stacked cf_{all}. The threshold for the G67 and G23 (cf_{12}) calculated according to the procedure described above is 0.3204 and that for G67, G23, and G29 (cf_{123}) is 0.3166.The threshold for cf_{all} is 0.2283 (Table 2). The detection results for both stacked *cf*s are shown in Figure 11b and c respectively, and summarized in Table 2. Focusing on the nearer stations basically increases the detection results as cf_{12} had 25 detections and cf_{123} had 17 detections in total. The four additional buried events detected by cf_{all} are also detected by cf_{12} and cf_{123}. Both cf_{12} and cf_{123} detect two addition low SNR events, and cf_{123} detects one more low SNR event. These events were not detected with cf_{all}. Figure 13a shows the waveforms of one of the events detected using both cf_{12} and cf_{123}, and Figure 13b shows the event that was detected only with cf_{123}. Waveforms of these events are noisier than those of the events detected by visual inspection shown in Figure 7, and it is difficult to identify their P-wave arrivals.

The detection from using cf_{12} includes 11 false alarms even though the number of false alarms with cf_{all} and cf_{123} was only 2. Focusing on the nearer stations should enhance sensitivity but at the same time detection results may include a lot of false alarms as in the case of cf_{12}. One reason could be that the number of the sensors is not enough to suppress the unexpected peaks that

445 occur at a few sensors. Once we find the best number of sensors to average, we can detect the
446 largest number of low SNR events having the minimum number of false alarms. The false alarms,
447 shown in Figure S3 and S4 (see supplemental materials), detected by both cf_{12} and cf_{123} (Fig. 11)
448 occur just after the M1.9 and M2.2 catalog events. This analysis suggests that focusing on the
449 nearer stations may provide better detection results than those obtained by including more distant
450 stations as cf_{all} does (see also Fig. S5 in supplemental materials).
451 For further comparison and validation of our method, we tested the STA/LTA method using
452 the same data. We set the STA and LTA windows to be 100 points (0.5 sec) and 500 points (2.5
453 sec) following the recommendation in Akram and Eaton, (2016). We then calculated STA/LTA
454 for all stations. Then, the STA/LTA time series are stacked using the same moveout that we used
455 for our method. We also set the threshold in the same manner as we have done for our new
456 method and we varied the subsets of stations used for the stacking. The results are summarized in
457 Table 2 STA/LTA can detect the two catalog events and 4 out of 6 events detected by visual
458 inspection. STA/LTA also detected some false alarms depending on the subset of stations used
459 for stacking. However, none of the low SNR events that were detected by our method were
460 detected by STA/LTA. As we discussed before, the KNMI network can detect more events than
461 in the catalog by using a method similar to STA/LTA. Human visual inspection outperforms
462 STA/LTA. Needless to say, our method detected more events than visual inspection and
463 STA/LTA. Complete details of detection results for our method are summarized in Table S1 and
464 compared with results obtained using STA/LTA and a simple template matching method.
465

466 **Conclusions**

467 To maximize the advantage of continuous recordings of microseismicity and for evaluating the
468 risks of potential significant induced seismic events, we need to detect as many events as
469 possible even from low SNR data. The event detection methods are required to detect even low

SNR events and diverse source types ideally without the use of template waveforms. We have proposed a novel event detection method designed to identify low SNR events by measuring polarization features that are independent of seismic source characteristics. Our method analyzes polarization in the time-frequency domain and extracts linearity and directionality of polarization. Linearly polarized signals coming from the direction of the reservoir are assumed to be seismic events. We applied this method to a small subset of induced seismicity monitoring data from Groningen, The Netherlands, and detected real events that are not in the public KNMI catalog. We also confirmed the performance of our method by comparison with human visual inspection and STA/LTA. Our method detects about twice as many events as STA/LTA and our method detects several additional events that human visual inspection missed. Thus, our method performed quite well at detecting low SNR events, so it can be used to complete existing seismic catalogs, which will lead to providing better characterization of reservoirs and better seismic risk assessment from the analysis of small magnitude events.

The current version of our method needs a previously observed reference event and we used its DOA and moveout information to focus detection on events from the region near that reference event. This requirement would be a technical challenge for the applicability of this method to a new field. However, we can overcome this by introducing forecasted DOA and moveout based on approaches such as waveform modeling (Dando et al. 2019). Then we could apply our method to the entire catalog to enhance it.

Data and Resources

Continuous data and the seismic catalog were obtained from KNMI website (http://rdsa.knmi.nl, last accessed on July, 2019).

Acknowledgments

This work was supported by ExxonMobil through its membership in the MIT Energy Initiative. We thank Brian deMartin for useful comments and data that contributed greatly to our work. We also thank KNMI for the seismic data. We are grateful to the constructive and encouraging comments from Dr. Volker Oye, an anonymous reviewer, and associate editor Eric Chael. We acknowledge Dr. Pawan Bharadwaj for useful discussions on signal processing, and also thank Dr. Rachel E. Abercrombie, and Dr. Florent Brenguier for useful discussion. This study was supported by JSPS Overseas Research Fellow (20160228) and ERL, MIT.

503 **References**

504 Akram, J., and D. Eaton (2016). A review and appraisal of arrival-time picking methods for
505 downhole microseismic data, *Geophysics* **81** 67–87. doi: 10.1190/GEO2014-0500.1.

506 Allen, R. V. (1978). Automatic earthquake recognition and timing from single traces. *Bull*.
507 *Seismol*. *Soc*. *Am*. **68** 1521–1532.

508 Baillard, C., W.C. Crawford, V. Ballu, C. Hibert, and A. Mangeney (2014). An automatic
509 kurtosis-based P-and S-phase picker designed for local seismic networks, *Bull*. *Seismol*. *Soc*.
510 *Am*. **104** 394–409. doi: 10.1785/0120120347.

511 Benhama, A., C. Cliet, and M. Dubesset (1988). Study and Applications of Spatial Directional
512 Filtering in Three-Component Recordings, *Geophys*. *Prospect*. **36** 591–613. doi:
513 10.1111/j.1365-2478.1988.tb02182.x.

514 Bourne, S.J., S.J. Oates, J. van Elk, and D. Doornhof (2014). A seismological model for
515 earthquakes induced by fluid extraction from a subsurface reservoir, *J*. *Geophys*. *Res*. *B*
516 *Solid Earth* **119** 8991–9015. doi: 10.1002/2014JB011663.

517 Dando, B.D.E., V. Oye, S.P.Näsholm, L.Zühlsdorff, D.Kühn, A.Wuestefeld (2019), Complexity
518 in microseismic phase identification: full waveform modelling, traveltime computations and
519 implications for event locations within the Groningen gas field, *Geophys*. *J*. *Int*. **217**, Issue
520 (1) 620–649, https://doi.org/10.1093/gji/ggz017.

521 Dost, B., F. Goutbeek, T. van Eck, and D. Kraaijpoel (2012). Monitoring induced seismicity in
522 the North of the Netherlands: status report 2010, *Technical Report*, Koninklijk Nederlands
523 Meteorologisch.

524 Dost, B., E. Ruigrok, and J. Spetzler (2017). Development of seismicity and probabilistic hazard
525 assessment for the Groningen gas field, *Geologie en Mijnbouw/Netherlands Journal of*
526 *Geosciences* **96** s235-s245. Doi: 10.1017/njg.2017.20.

527 Frohlich, C. (1992). Triangle diagrams: ternary graphs to display similarity and diversity of

earthquake focal mechanisms, *Phys*. *Earth*. *Planet*. *Inter*. **75** 193–198. doi: 10.1016/0031-9201(92)90130-N.

Gharti,H. N., V. Oye, M. Roth, and D. Kühn (2010). Automated microearthquake location using envelope stacking and robust global optimization, *Geophysics* **75**: MA27-MA46.

Gibbons, S.J., and F. Ringdal (2006). The detection of low magnitude seismic events using array-based waveform correlation, *Geophys*. *J*. *Int*. **165** 149–166. doi: 10.1111/j.1365-246X.2006.02865.x.

Huang, Y., and G.C. Beroza (2015). Temporal variation in the magnitude-frequency distribution during the Guy-Greenbrier earthquake sequence, *Geophys*. *Res*. *Lett*. **42** 6639–6646. doi: 10.1002/2015GL065170.

Langet, N., A., Maggi, A., Michelini, and F., Brenguier (2014). Continuous Kurtosis-Based Migration for Seismic Event Detection and Location, with Application to Piton de la Fournaise Volcano, La Reunion, *Bull*. *Seismol*. *Soc*. *Am*. **104** 229–246. doi: 10.1785/0120130107.

Meersman, K. D., M. van der Baan, and J.-M. Kendall (2006). Signal Extraction and Automated Polarization Analysis of Multicomponent Array Data, *Bull*. *Seismol*. *Soc*. *Am*. **96** (6): 2415–2430, https://doi.org/10.1785/0120050235.

Moriya, H. (2008). Precise arrival time detection of polarized seismic waves using the spectral matrix, *Geophys*. *Prospect*. **56**:667–676. doi: 10.1111/j.1365-2478.2008.00713.x.

Moriya, H., and H. Niitsuma (1996). Precise detection of a P-wave in low S/N signal by using time-frequency representations of a triaxial hodogram, *Geophysics* **61** 1453. doi: 10.1190/1.1444071.

Nagano, K., H. Niitsuma, and N. Chubachi (1989). Automatic algorithm for triaxial hodogram source location in downhole acoustic emission measurement, *Geophysics* **54**, 508–513, http://dx.doi.org/10.1190/1.1442677.

553 Oye, V. and W. L. Ellsworth (2005). Orientation of Three-Component Geophones in the San
554 Andreas Fault Observatory at Depth Pilot Hole, Parkfield, California, *Bull*. *Seismol*. *Soc*.
555 *Am*. **95** (2): 751–758.
556 Poliannikov, V.O. and M. C. Fehler (2018). Instantaneous phase-based statistical method for
557 detecting seismic events with application to Groningen gas field data, *SEG Technical*
558 *Program Expanded Abstracts 2018* pp. 2907-2911.
559 Shapiro, N.M., and M. Campillo (2004). Emergence of broadband Rayleigh waves from
560 correlations of the ambient seismic noise, *Geophys*. *Res*. *Lett*. **31**:8–11. doi:
561 10.1029/2004GL019491.
562 Shelly R.D., G.C. Beroza, and S. Ide (2007). Non-volcanic tremor and low-frequency earthquake
563 swarms, *Nature* **446** 305–307. doi: 10.1038/nature05666.
564 Skoumal J.R., M.R. Brudzinski, B.S. Currie, and J. Levy (2014). Optimizing multi-station
565 earthquake template matching through re-examination of the Youngstown, Ohio, sequence,
566 *Earth*. *Planet*. *Sci*. *Lett*. **405** 274–280. doi: 10.1016/j.epsl.2014.08.033.
567 Samson J. C., (1977), Matrix and Stokes velocity representations of detectors for polarized
568 waveforms: Theory, with some applications to teleseismic waves, *Geophys*. *J*. *Roy*. *Astr*.
569 *Soc*. **51**, 583–603.
570 Shearer P. M., (1999), Introduction to Seismology, Cambridge, New York, Melbourne:
571 Cambridge University Press.
572 Soma, N., H. Niitsuma, and R. Baria (2007). Reflection imaging of deep reservoir structure
573 based on three-dimensional hodogram analysis of multicomponent microseismic waveforms,
574 *J*. *Geophys*. *Res*. *Solid Earth* **112** 1–14. doi: 10.1029/2005JB004216.
575 Soma, N., H. Niitsuma, and R. Baria (2002). Reflection technique in time-frequency domain
576 using multicomponent acoustic emission signals and application to geothermal reservoirs,
577 *Geophysics* **67** 928–938. doi: 10.1190/1.1484535.

578 Spetzler, J., and B. Dost (2017). Hypocenter estimation of induced earthquakes in Groningen,
579 *Geophys*. *J*. *Int*. **209** 435–465. doi: 10.1093/gji/ggx020.
580 Templeton, C. D., J., Wang, K. M., Goebel, B. D. Harris, and T. T., Cladouhos (2020). Induced
581 seismicity during the 2012 Newberry EGS stimulation: Assessment of two advanced
582 earthquake detection techniques at an EGS site, *Geothermics* **83**.
583 https://doi.org/10.1016/j.geothermics.2019.101720.
584 Van Eck, T., F. H. Goutbeek, H. Haak and B. Dost, 2004. Seismic hazard due to small shallow
585 induced earthquakes, KNMI-Scientific report WR-2004-01, 52pp.
586 Walters, R. J., Zoback, M. D., Baker, J. W., & Beroza, G. C. (2015). Characterizing and
587 responding to seismic risk associated with earthquakes potentially triggered by fluid
588 disposal and hydraulic fracturing. *Seismol Res Lett*, **86**(4), 1110–1118.
589 https://doi.org/10.1785/0220150048.
590 Willacy, C., E. van Dedem, S. Minisini, J. Li, J.W. Blokland, I. Das, and A. Droujinine (2018).
591 Application of full-waveform event location and moment-tensor inversion for Groningen
592 induced seismicity. *Lead*. *Edge*. **37** 92–99. doi: 10.1190/tle37020092.1.
593 Withers, M., R. Aster, C. Young, J. Beiriger, M. Harris, S. Moore, and J. Trujillo (1998). A
594 comparison of select trigger algorithms for automated global seismic phase and event
595 detection. *Bull*. *Seismol*. *Soc*. *Am*. **88** 95–106.
596 Wu, J., D. Yao, X. Meng, Z. Peng, J. Su, and F. Long (2017). Spatial-temporal evolutions of
597 early aftershocks following the 2013 Mw6.6 Lushan earthquake in Sichuan, China. *J*.
598 *Geophys*. *Res*. *Solid Earth* **122**:2873–2889. doi: 10.1002/2016JB013706.
599

600 **Full mailing address for each author**

601

602 Earth Resources Laboratory, Department of Earth, Atmospheric and Planetary Sciences,
603 Massachusetts Institute of Technology,
604 77 Massachusetts Avenue Cambridge, Massachusetts 02139-4307, USA
605 mukuhira@mit.edu, poliann@mit.edu, fehler@mit.edu,
606 (**Yusuke Mukuhira**, **Oleg V. Poliannikov**, **Michael C. Fehler**)

607

608 Current affiliation: Institute of Fluid Science, Tohoku University,
609 2-1-1 Katahira, Aoba-ku, Sendai, 980-8577, Japan
610 mukuhira@tohoku.ac.jp (**Yusuke Mukuhira**)

611

612 School of Engineering, Tohoku University,
613 6-6-04 Aramaki aza aoba, Aoba-ku, Sendai, 980-8579, Japan
614 hirokazu.moriya.e1@tohoku.ac.jp, (**Hirokazu Moriya**)

615

Tables

Table 1. Summary of analysis conditions.

	Synthetic wave test (Fig. S1)	**SNR sensitivity analysis (Fig. 3)**	**Catalog event: M1.9 (Fig. 5)**	**Undetected event (Fig. 6)**	**Influence of window length (Fig. 7)**	**Detection (Fig. 8, 10-13)**
Wave	Synthetic wave sinusoidal plus band limited noise	Synthetic wave sinusoidal plus various SNR band limited noise	Real seismogram	Real seismogram	Real seismogram	Real seismogram
Sampling frequency	100 Hz	100 Hz	200 Hz	200 Hz	200 Hz	200 Hz
Time window	20 points (0.2 sec)	20 points (0.2 sec)	50 points (0.25 sec)	50 points (0.25 sec)	20, 50, 100, 150, 200 points	50 points (0.25 sec)
Time window shift	1 point	NA	1 point	1 point	1 point	1 point
Frequency band	0-50 Hz	0-50 Hz	0-100 Hz	0-100 Hz	0-100 Hz	0-100 Hz
Averaged frequency band	5-15 Hz	5-15 Hz	20-40 Hz	20-40 Hz	20-40 Hz	20-40 Hz

621 **Table 2.** The result of event detection with different ways of stacking *cf*. B1~6 are the low SNR
622 events detected by visual inspection, which we used as benchmarks to show that our method has
623 detectability that is better than visual inspection. As another benchmark, the result of detection
624 with STA/LTA method is also shown.

625

	Our method			**STA/LTA**		
	Stacked all: cf_{all} (0.2283)	Stacked 1-2: cf_{12} (0.3204)	Stack 1-3: cf_{123} (0.3166)	Stacked all: STA/LTA_{all} (0.2337)	Stacked 1-2: STA/LTA_{12} (0.2821)	Stack 1-3: STA/LTA_{123} (0.2556)
Catalog M1.9	detected	detected	detected	detected	detected	detected
Catalog M2.2	detected	detected	detected	detected	detected	detected
B1	detected	detected	detected	detected	detected	detected
B2	detected	detected	detected			
B3	detected	detected	detected	detected	detected	detected
B4	detected	detected	detected	detected	detected	detected
B5	detected	detected	detected	detected	detected	detected
B6	detected	detected	detected			
Additional low SNR events	4	6	7	0	0	0
False alarms	2	11	2	1	0	1
Total	14	25	17	7	6	7

626

627

628 **List of Figure Captions**

629 **Figure 1.** Examples of particle motions around several phases. The waveforms shown with white
630 lines are the 3 component seismograms of M1.9 catalog event recorded at G674 Groningen, the
631 Netherlands. The background images behind waveforms are spectrograms (horizontal-1,
632 horizontal-2 and vertical component from top to bottom). Particle motions shown in sub-panels
633 are plotted with samples within hatched time windows for noise, P-wave arrival, S-wave arrival,
634 possible converted or reflected wave, and S-coda part. Note that the scales of each cube are
635 different.

636

637 **Figure 2**. Conceptual image of the linear particle motion (bold black line). This linear particle
638 motion is expressed as the 1st eigenvector (V_1) shown with a red arrow. The angle between V_1
639 and the horizontal plane is defined as DOA inclination, which is estimated with equation (5). In
640 many cases, the orientation of the horizontal axes are not known, so DOA azimuth is not used in
641 this study.

642

643 **Figure 3**. The result of SNR sensitivity analysis. (a) example of synthetic waveforms in the case
644 of SNR = -1.9 dB. The $\overline{C_L}$ for the noise part is estimated from the blue hatched area and the $\overline{C_L}$
645 for the P-wave part is estimated from the red hatched area. (b) Distribution of $\overline{C_L}$ for noise (blue)
646 and P-wave part (red) for various values of SNR (10, 5, 0, -5, -7, and -10 dB). Histograms
647 describe probability density functions (PDF).

648

649 **Figure 4.** Map of the study area. Left shows The Netherlands and the location of the Groningen
650 Field (dark shading). Right is the plan view of our study area. The locations of the M1.9 and
651 M2.2 catalog events are shown with red stars. The depths of both catalog events are 3km.
652 Locations determined by the Royal Netherlands Meteorological Institute (KNMI) are Lat.

53.3010, Long. 6.8070 (M1.9 event), and Lat. 53.3060, Long. 6.8090 (M2.2 event). Five stations used in this study are shown with green markers showing station names. The distances from the epicenter of the M2.2 event to each station are 1.9386 km (G67), 2.7917 km (G23), 3.1065 km (G29), 3.5810 km (G19), and 3.6155 km (G24).

Figure 5. The result for linearity (C_L) and DOA inclination (DOA_{inc}) on M1.9 catalog event. (a) 3-component waveforms at the 4th level (200 m depth) at station G67. Blue and red are horizontal components, and yellow is vertical component. Time in sequence is referenced to the beginning of our data window at 00:00:00.315 on 1st November 2016. (b) C_L distribution in time and frequency. (c) $\overline{C_L}$ averaged over 20~40 Hz. (d) DOA_{inc} distribution in time and frequency. (e) $\overline{DOA_{inc}}$ averaged over 20~40 Hz.

Figure 6. The evaluation result of linearity (C_L) and DOA inclination (DOA_{inc}) on low SNR event detected by our visual inspection. Details are the same as those for Figure 5.

Figure 7. Influence of the window length on $\overline{C_L}$ and $\overline{DOA_{inc}}$. (a) 3 component waveforms of low SNR event (the same event in Fig. 6). (b) $\overline{C_L}$ estimated with different window lengths. Lengths tested here are shown with different colors. Blue: 20 points (0.1 sec), Red: 50 points (0.25 sec), Yellow: 100 points (0.5 sec), Purple: 150 points (0.75 sec), Green: 200 samples (1.0 sec). Red line is the result of window length used in this study. (c) $\overline{DOA_{inc}}$ results. Color code is same as (b).

Figure 8. The performance of our characteristic function for detection purpose. (a) 3 component waveforms of low SNR event (same event in Fig. 6 and 7). (b) timeseries of $\overline{C_L}$. (c) blue:

timeseries of $\overline{DOA_{inc}}$. red: Characteristic function for DOA inclination (C_{DOA}). (d) Characteristic function for event detection.

Figure 9. Moveout used to stack *cf*s. The reference station is G674 (deepest sensor at G67). This moveout was estimated in Poliannikov and Fehler, (2018).

Figure 10. (a) The *cf*s estimated for 4 hours of continuous data. Color indicates monitoring well. Each monitoring well has four downhole seismometers (50, 100, 150, 200m). The *cf*s are plotted in the order of depth. (b) Stacked *cf* using the moveout shown in Figure 9.

Figure 11. Results of detection with our proposed method. Stars: catalog M1.9 and M2.2 events. Diamonds: low SNR events detected by visual inspection. Triangles: low SNR events detected by our method. Open triangles: false alarms detected by our method. (a) Stacked *cf* for all stations and the detection results with cf_{all}. (b) Stacked *cf* for G67 and G23 (cf_{12}) and the detection result with cf_{12}. (c) Stacked *cf* for G67, G23, and G29 (cf_{123}), and the detection result with cf_{123}.

Figure 12. Examples of waveforms of detected low SNR events. Both events are detected by our method with cf_{all}, cf_{12}, and cf_{123} but not by visual inspection. Occurrence time of these events can be seen in Figure 11 with triangle markers or Table S1. Black lines are the onset of detection at the 4^{th} level (200 m) sensor at G67 station.

Figure 13. Examples of waveforms of detected low SNR events. Both events are not detected with cf_{all} nor with visual inspection. Occurrence time of these events can be seen in Figure 11 with triangle markers or Table S1. (a) the low SNR event detected with cf_{12} and cf_{123}. (b) the low

SNR event detected only by cf_{123}. Black lines are the onset of detection at the 4th level (200 m) sensor at G67 station.

Figure

Click here to access/download;Figure;BSSAmuku2019Figure8_afterReview2.docx

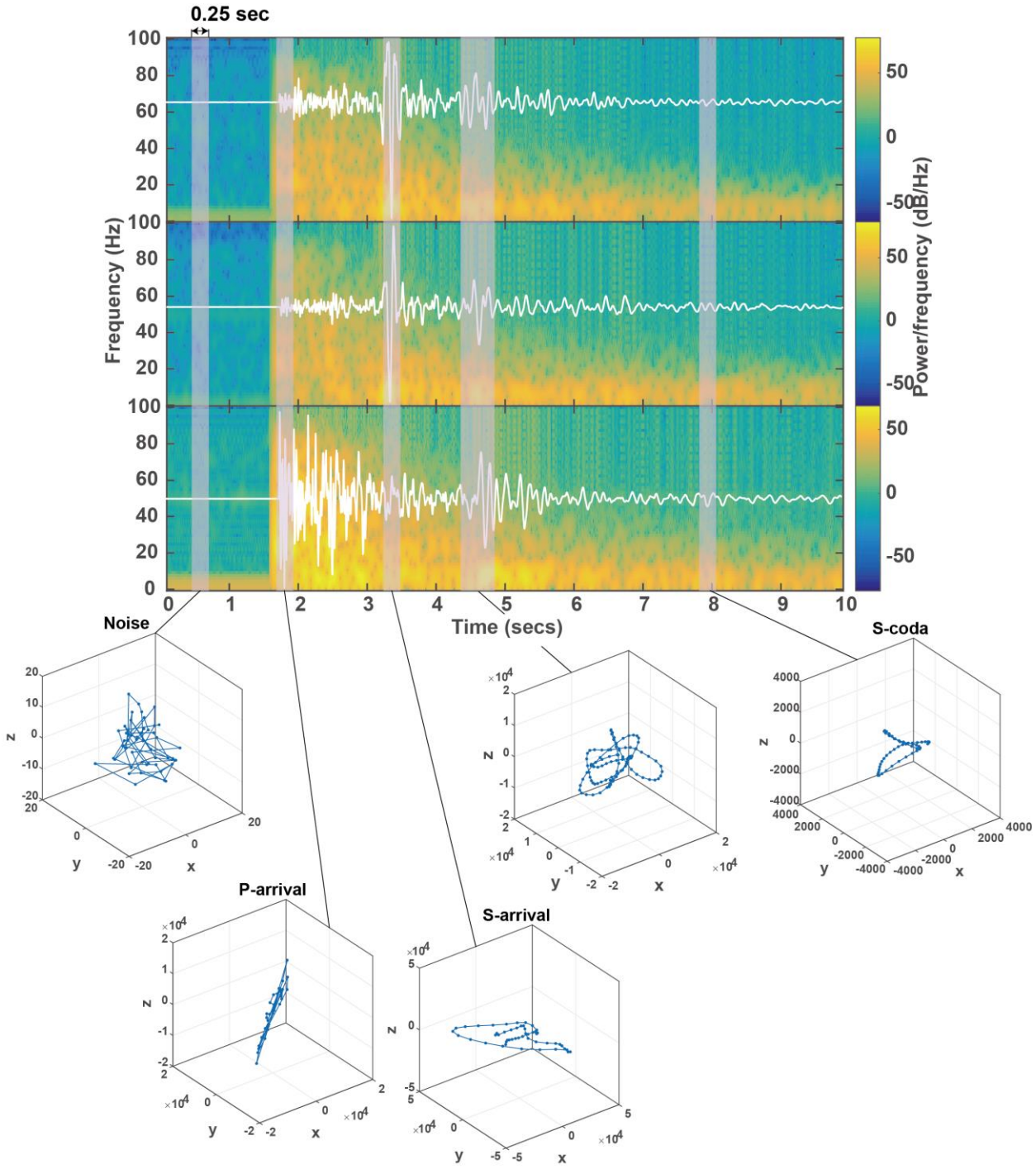

Figure 1. Examples of particle motions around several phases. The waveforms shown with white lines are the 3 component seismograms of M1.9 catalog event recorded at G674 Groningen, the Netherlands. The background images behind waveforms are spectrograms (horizontal-1, horizontal-2 and vertical component from top to bottom). Particle motions shown in sub-panels are plotted with samples within hatched time windows for noise, P-wave arrival, S-wave arrival, possible converted or reflected wave, and S-coda part. Note that the scales of each cube are different.

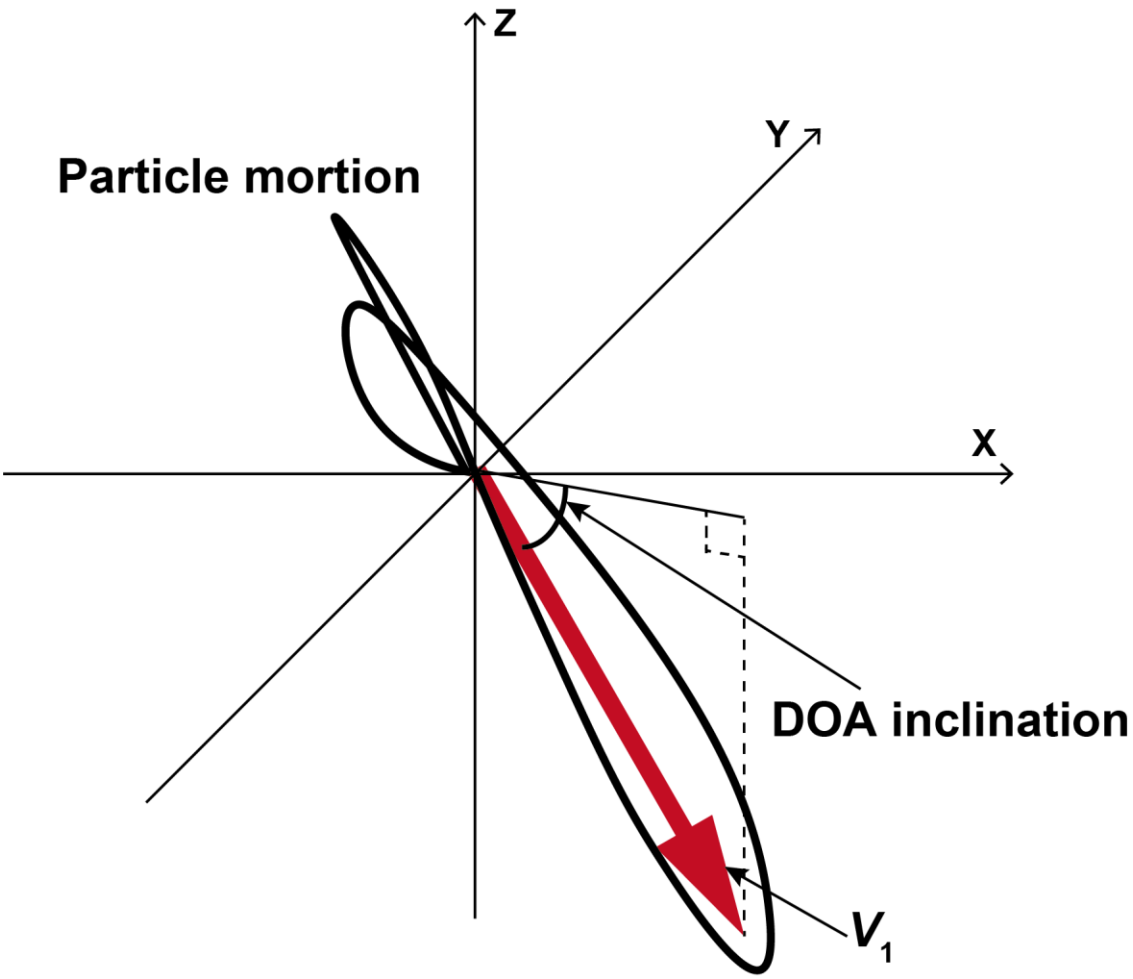

Figure 2. Conceptual image of the linear particle motion (bold black line). This linear particle motion is expressed as the 1st eigenvector (V_1) shown with a red arrow. The angle between V_1 and the horizontal plane is defined as DOA inclination, which is estimated with equation (5). In many cases, the orientation of the horizontal axes are not known, so DOA azimuth is not used in this study.

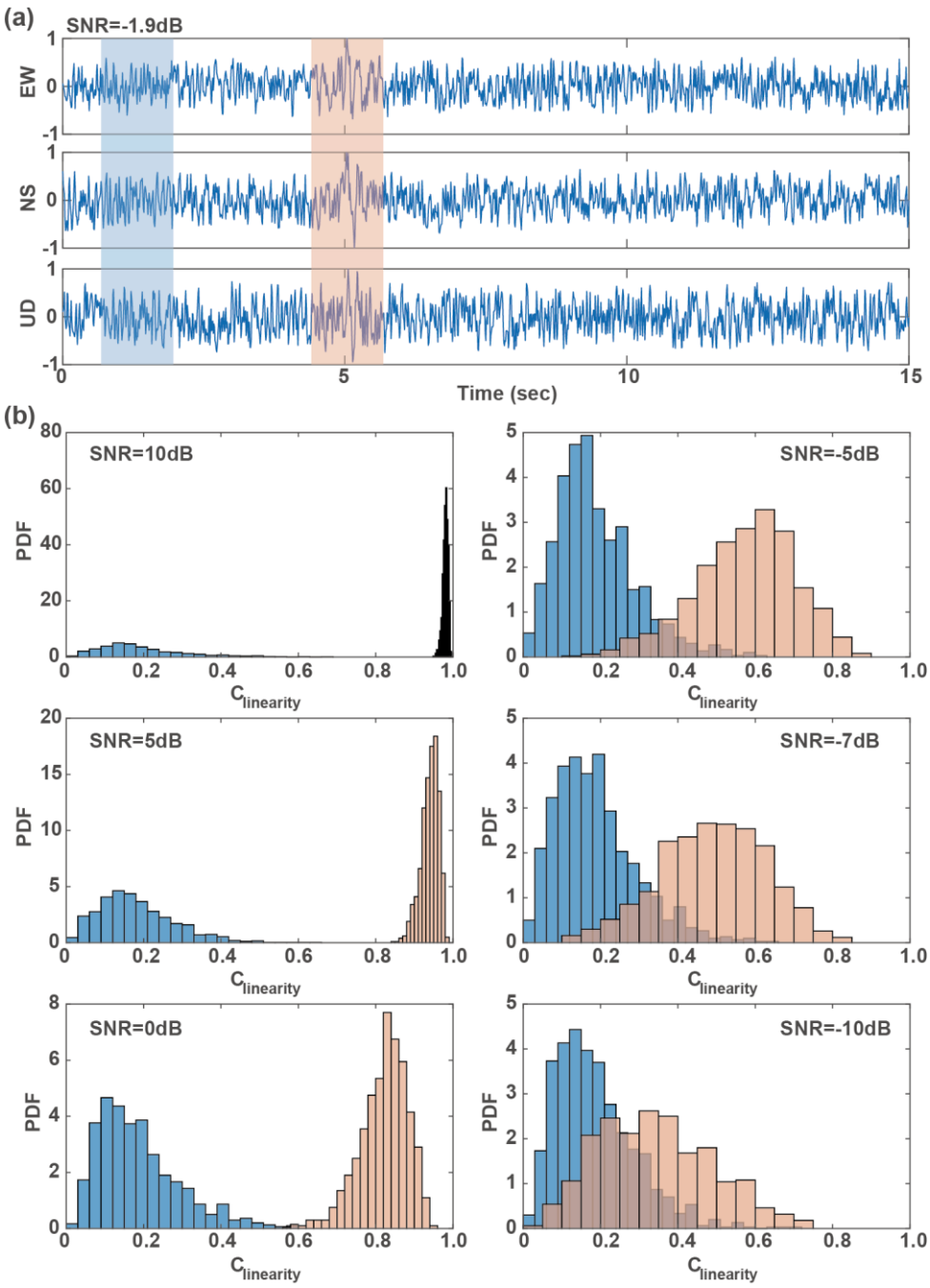

Figure 3. The result of SNR sensitivity analysis. (a) example of synthetic waveforms in the case of SNR = -1.9 dB. The $\overline{C_L}$ for the noise part is estimated from the blue hatched area and the $\overline{C_L}$ for the P-wave part is estimated from the red hatched area. (b) Distribution of $\overline{C_L}$ for noise (blue) and P-wave part (red) for various values of SNR (10, 5, 0, -5, -7, and -10 dB). Histograms describe probability density functions (PDF).

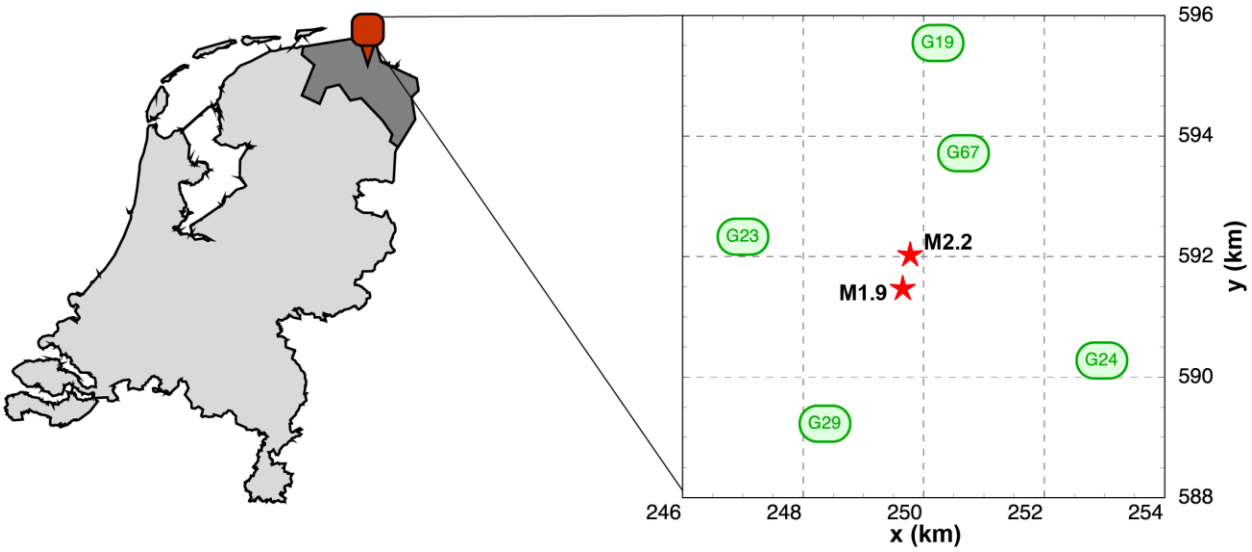

Figure 4. Map of the study area. Left shows The Netherlands and the location of the Groningen Field (dark shading). Right is the plan view of our study area. The locations of the M1.9 and M2.2 catalog events are shown with red stars. The depths of both catalog events are 3km. Locations determined by the Royal Netherlands Meteorological Institute (KNMI) are Lat. 53.3010, Long. 6.8070 (M1.9 event), and Lat. 53.3060, Long. 6.8090 (M2.2 event). Five stations used in this study are shown with green markers showing station names. The distances from the epicenter of the M2.2 event to each station are 1.9386 km (G67), 2.7917 km (G23), 3.1065 km (G29), 3.5810 km (G19), and 3.6155 km (G24).

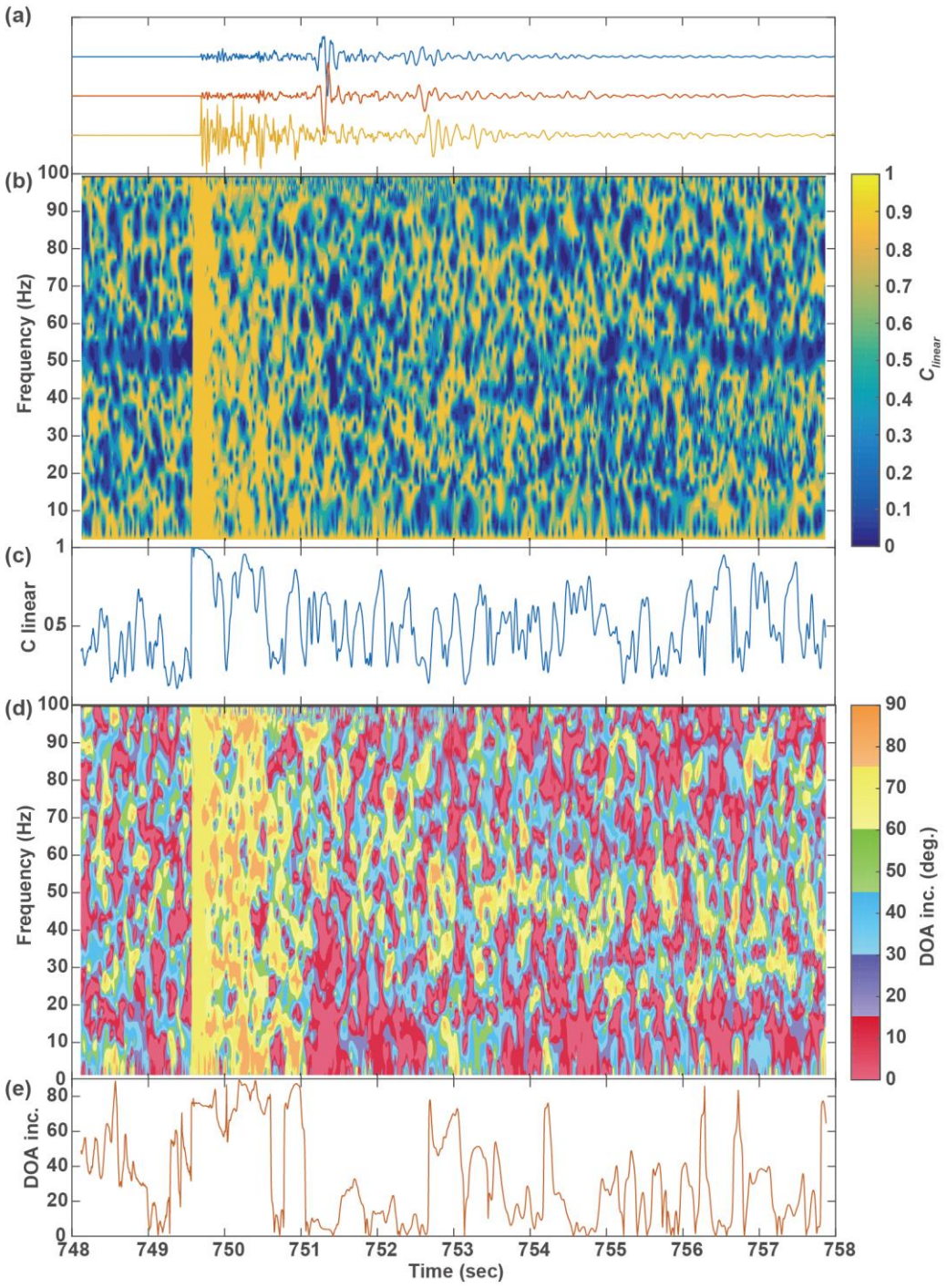

Figure 5. The result for linearity (C_L) and DOA inclination (DOA_{inc}) on M1.9 catalog event. (a) 3-component waveforms at the 4th level (200 m depth) at station G67. Blue and red are horizontal components, and yellow is vertical component. Time in sequence is referenced to the beginning of our data window at 00:00:00.315 on 1st November 2016. (b) C_L distribution in time and frequency. (c) $\overline{C_L}$ averaged over 20~40 Hz. (d) DOA_{inc} distribution in time and frequency. (e) $\overline{DOA_{inc}}$ averaged over 20~40 Hz.

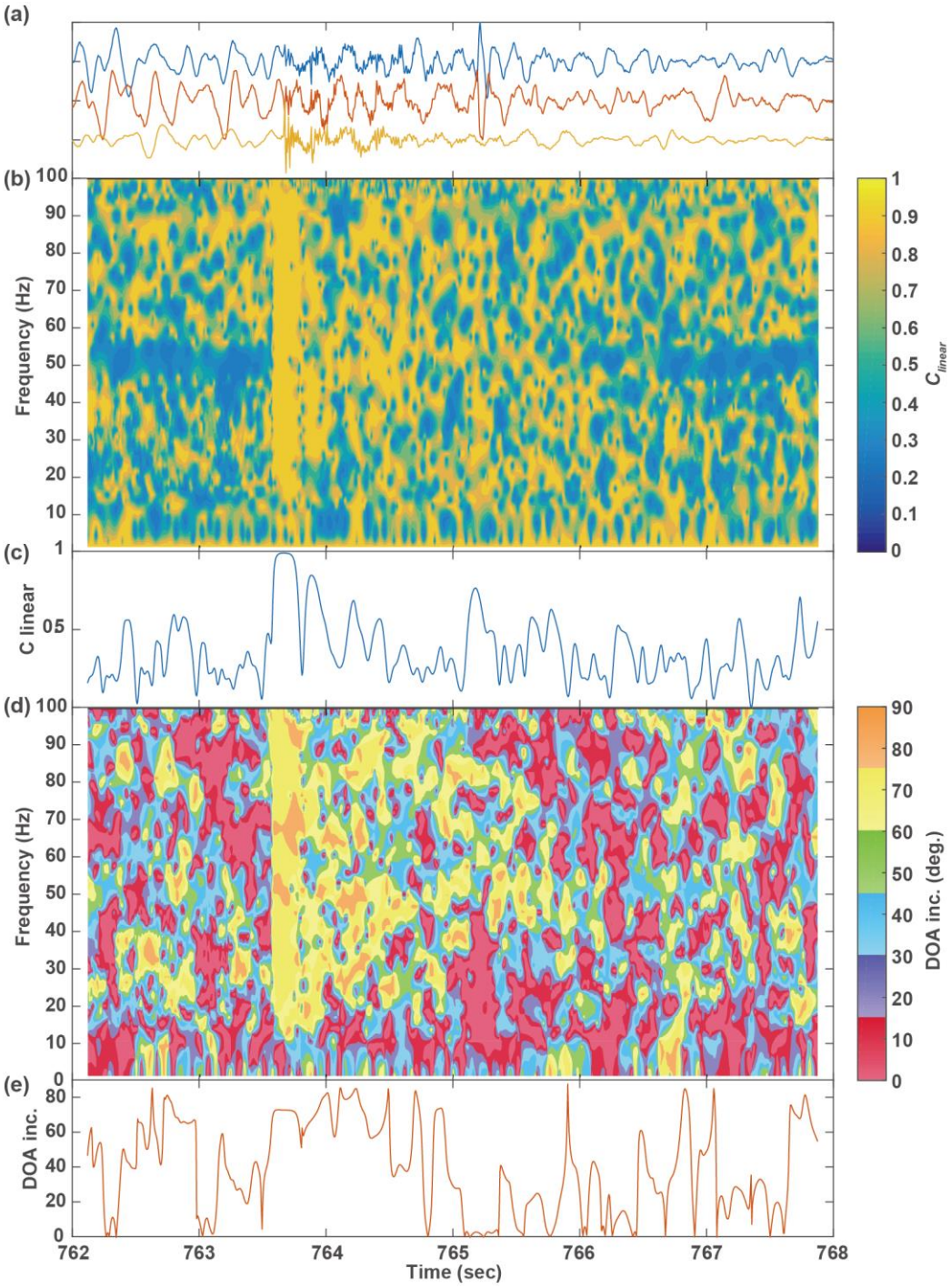

Figure 6. The evaluation result of linearity (C_L) and DOA inclination (DOA_{inc}) on low SNR event detected by our visual inspection. Details are the same as those for Figure 5.

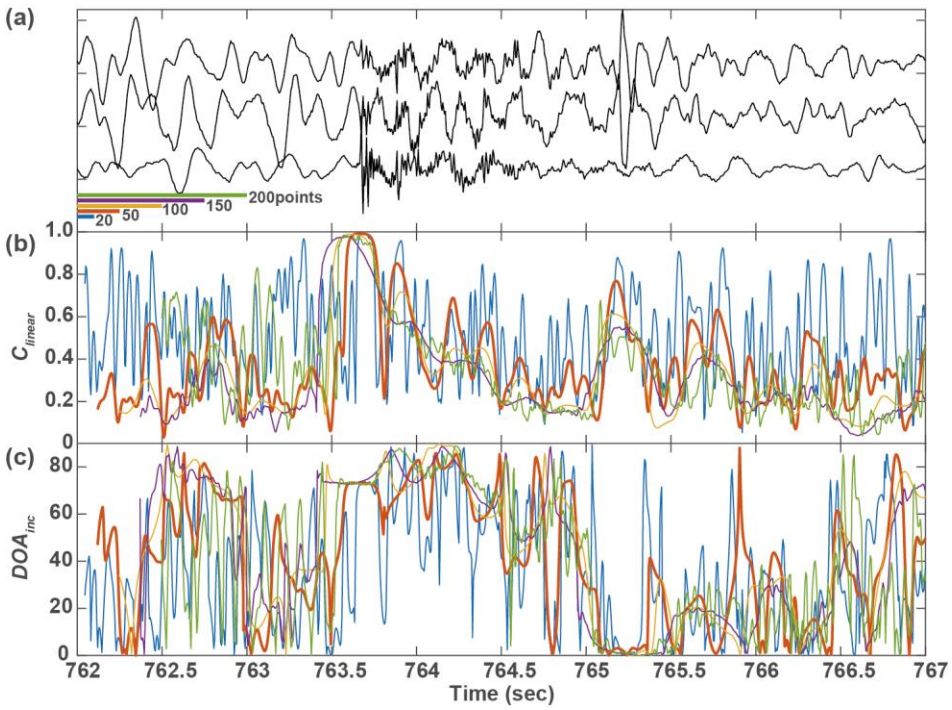

Figure 7. Influence of the window length on $\overline{C_L}$ and $\overline{DOA_{inc}}$. (a) 3 component waveforms of low SNR event (the same event in Fig. 6). (b) $\overline{C_L}$ estimated with different window lengths. Lengths tested here are shown with different colors. Blue: 20 points (0.1 sec), Red: 50 points (0.25 sec), Yellow: 100 points (0.5 sec), Purple: 150 points (0.75 sec), Green: 200 samples (1.0 sec). Red line is the result of window length used in this study. (c) $\overline{DOA_{inc}}$ results. Color code is same as (b).

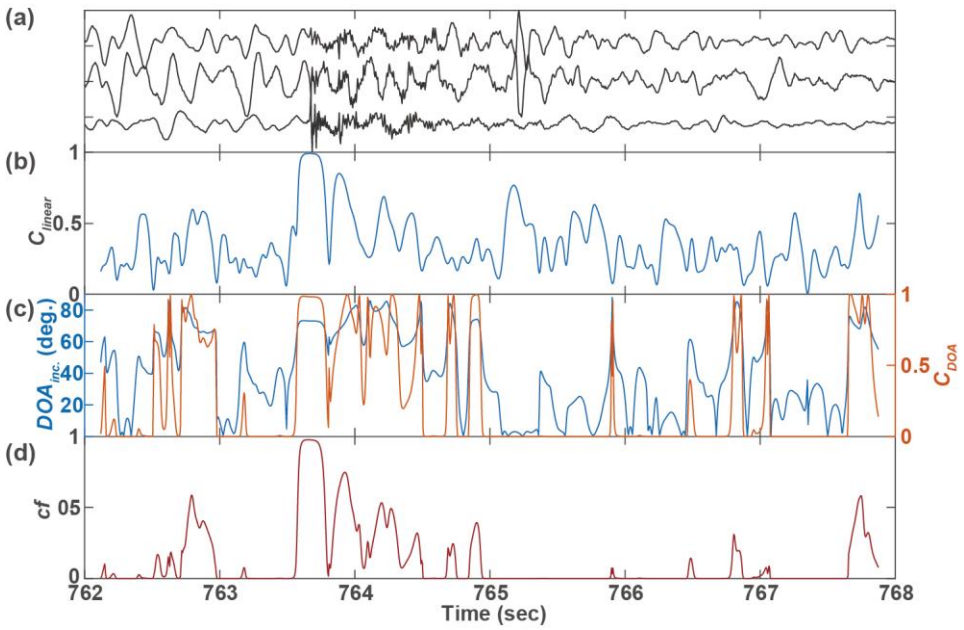

Figure 8. The performance of our characteristic function for detection purpose. (a) 3 component waveforms of low SNR event (same event in Fig. 6 and 7). (b) timeseries of $\overline{C_L}$. (c) blue: timeseries of $\overline{DOA_{inc}}$. red: Characteristic function for DOA inclination (C_{DOA}). (d) Characteristic function for event detection.

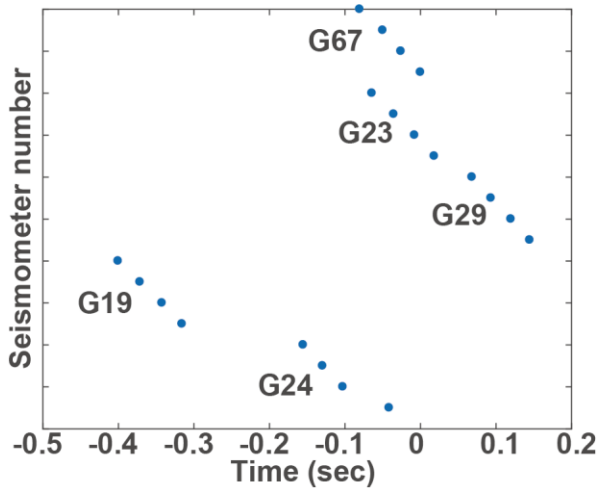

Figure 9. Moveout used to stack *cf*s. The reference station is G674 (deepest sensor at G67). This moveout was estimated in Poliannikov and Fehler, (2018).

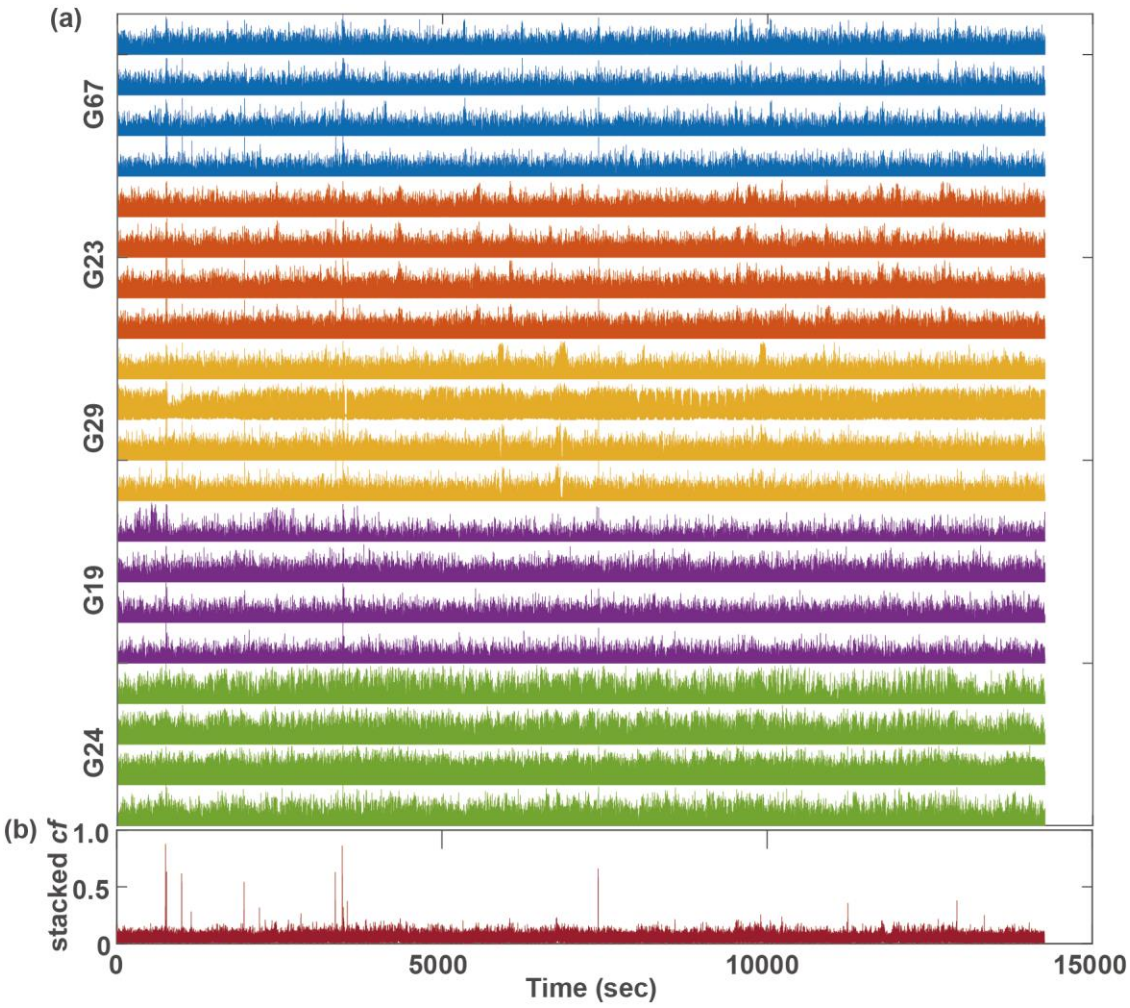

Figure 10. (a) The *cf*s estimated for 4 hours of continuous data. Color indicates monitoring well. Each monitoring well has four downhole seismometers (50, 100, 150, 200m). The *cf*s are plotted in the order of depth. (b) Stacked *cf* using the moveout shown in Figure 9.

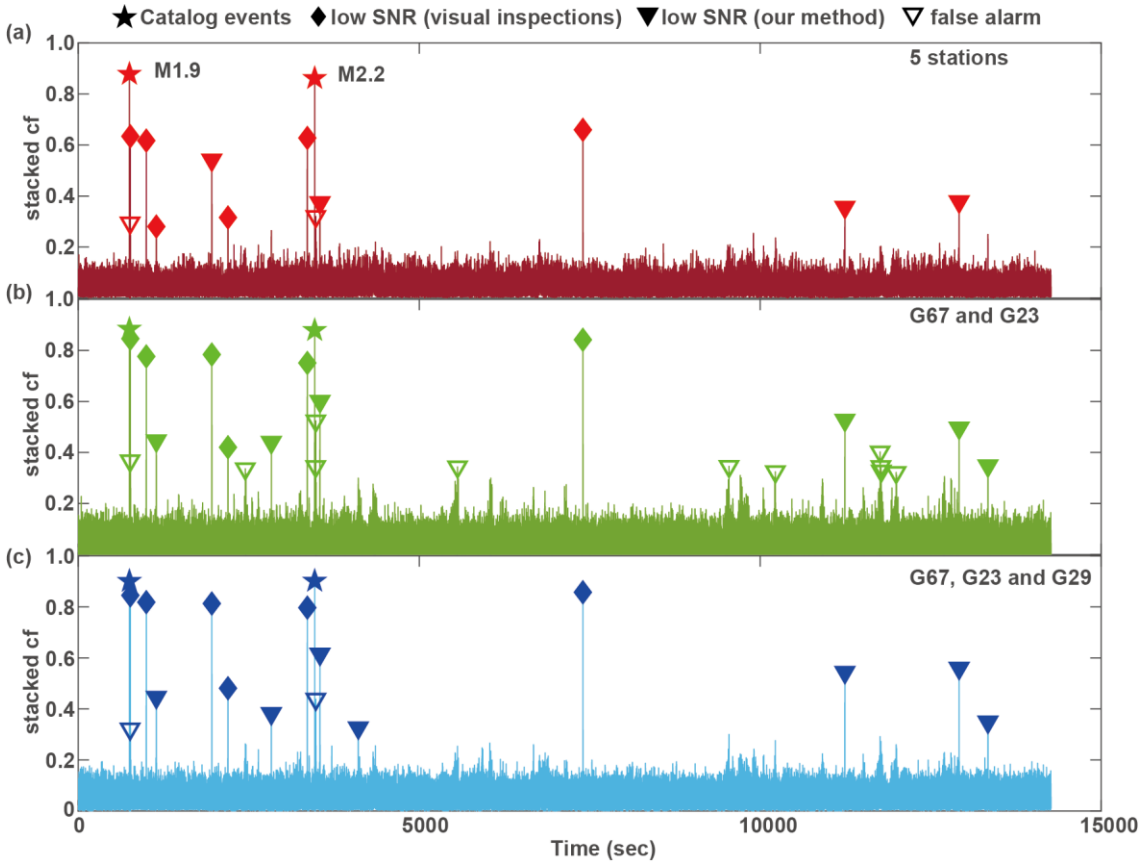

Figure 11 Results of detection with our proposed method. Stars: catalog M1.9 and M2.2 events. Diamonds: low SNR events detected by visual inspection. Triangles: low SNR events detected by our method. Open triangles: false alarms detected by our method. (a) Stacked *cf* for all stations and the detection results with cf_{all}. (b) Stacked *cf* for G67 and G23 (cf_{12}) and the detection result with cf_{12}. (c) Stacked *cf* for G67, G23, and G29 (cf_{123}), and the detection result with cf_{123}.

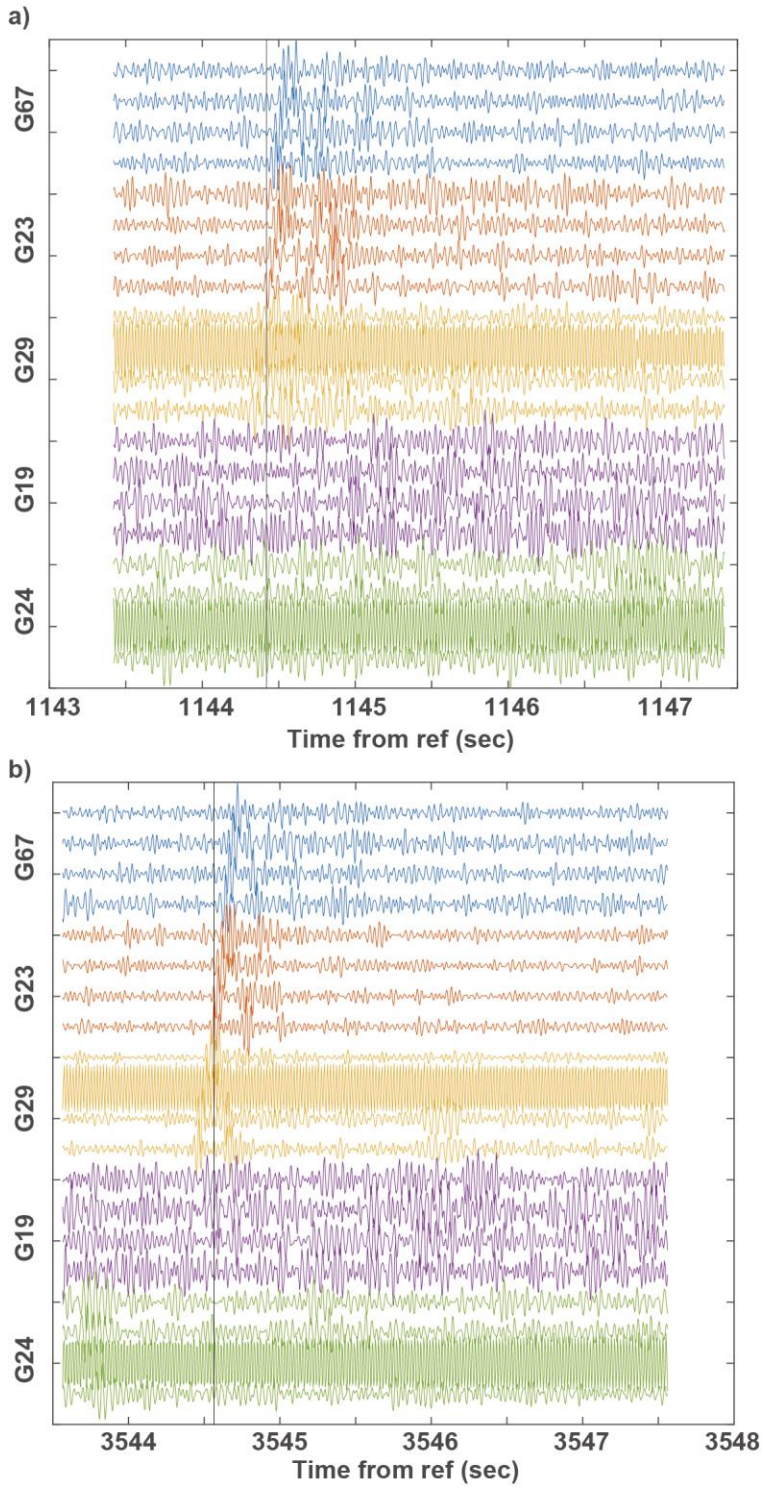

Figure 12. Examples of waveforms of detected low SNR events. Both events are detected by our method with cf_{all}, cf_{12}, and cf_{123} but not by visual inspection. Occurrence time of these events can be seen in Figure 11 with triangle markers or Table S1. Black lines are the onset of detection at the 4th level (200 m) sensor at G67 station.

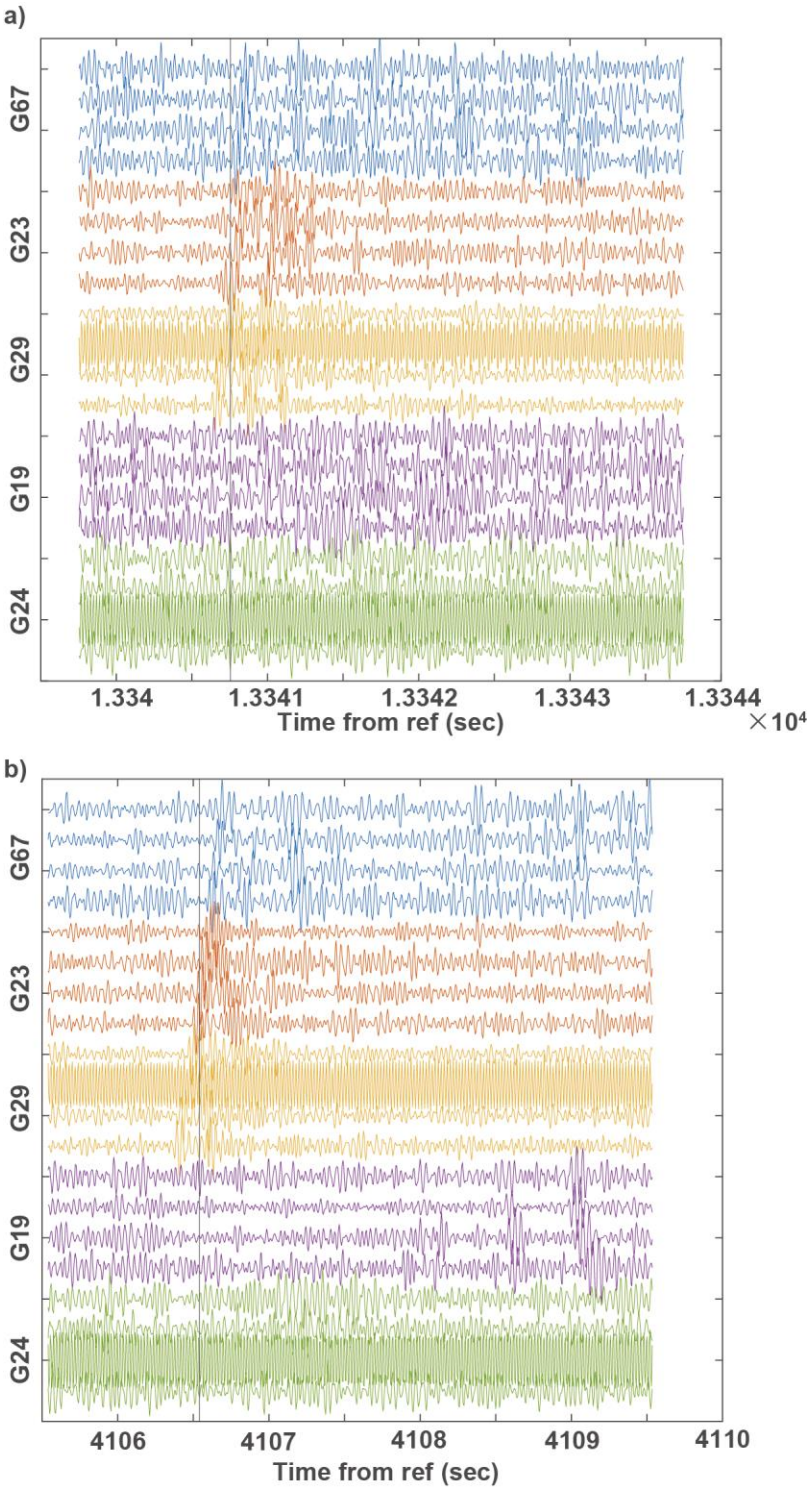

Figure 13. Examples of waveforms of detected low SNR events. Both events are not detected with cf_{all} nor with visual inspection. Occurrence time of these events can be seen in Figure 11 with triangle markers or Table S1. (a) the low SNR event detected with cf_{12} and cf_{123}. (b) the low SNR event detected only by cf_{123}. Black lines are the onset of detection at the 4th level (200 m) sensor at G67 station.

BSSA

Supplemental material for

Low SNR microseismic detection using direct *P*-wave arrival polarization

Yusuke Mukuhira*, Oleg V. Poliannikov, Michael C. Fehler, and Hirokazu Moriya

*Corresponding author: Yusuke Mukuhira (mukuhira@tohoku.ac.jp)

Description of the Supplemental Material

This supplemental material contains following five figures.

- Figure S1 showing the performance of our method for synthetic 3C signal.
- Figure S2 showing the characteristic function for equation (7).
- Figure S3 and S4 showing the examples of false alarm events detected by our method.
- Figure S5 showing the summary of the performance of our method.

We present the detail methodology and the result of syntethic wave test, which is used in the tests using syntethic signals section in main manuscript.

We discussed the performance of our method in the Discussion section, and we mentioned that, when using cf_{12} and cf_{123}, our method detected two false alarms occurring immediately after the M1.9 and M2.2 catalog events. We interpreted them as either coherent reflections or converted waves. The waveforms of these two false alarms are shown in Figures S3 and S4.

We also present the additional discussion about the performance of our method in Figure S5. This discussion is not included in the main text since the discussion here is qualitative. This is merely one way to evaluate the performance of our method.

Further comparisons of the detection performance between our method, STA/LTA and template matching methods are given in Table S1 along with the description of the template matching method test.

Supplemental Text

1. Synthetic wave test

To test our estimators of linearity and DOA, we conduct a simple synthetic study. We generate synthetic P- and S-wave arrival recordings for a 3C sensor. The source function is one cycle of a sinusoidal wave with a center frequency of 10 Hz. The recorded data are contaminated with additive band limited noise (Fig. S1). The phases of the 3C data components are shifted so that the true DOA inclination angle is 50° (Fig. S1a). Data are sampled at 100 Hz. We compute the SPM matrix using STFT with a 20-point (0.2 s) moving time window and a 1-point time shift. We decompose the SPM matrix for each time window and each quantized frequency and estimate C_L and $\bar{\theta}$. Figure S1b and d show estimates of C_L and $\bar{\theta}$ in the time-frequency domain. There is a clear peak of linearity around the time of the P-wave arrival. The peak starts a little bit earlier than the exact arrival time of the P-wave due to the finite width of the moving time window. We can also observe that the color around the P-wave arrival and 10 Hz corresponds to DOA of about 50°. The mean values of C_L and $\bar{\theta}$ are calculated by averaging C_L and $\bar{\theta}$ from 5 to 15 Hz, and shown in Figure S1c and e. $\overline{C_L}$ and $\bar{\theta}$ show the high linearity and the correct DOA inclination angle respectively at the time of the P-wave arrival. The proposed method therefore performs as intended on our simple synthetic example.

2. Simple template matching (cross correlation) test

For more comparison of our method with recent template matching methods (e.g., Gibbons and Ringdal 2006; Skoumal et al. 2014; Huang and Beroza 2015), we employed a simple template matching method. We used the entire waveforms of two (M1.9 and M2.2) catalog events. For simple computation, we selected a 10-sec common time window containing the event waveforms on all seismometers. These time windows contain P-wave, S-wave, and S-coda of the template waveforms on the vertical component. Windows start from 748 to 758 sec and 3466 - 3476 from reference time (00:00:00.315 on 1st November 2016) for the M1.9 and M2.2 events, respectively. We compute the cross correlation coefficient (CC) between the reference wave windows and a moving time window of the same size. Since we use the same time window for all sensors, we can stack CC values among stations without moveout. Then, we set the threshold for detection in the same manner described for our method. Note that in the CC case we defined the thresholds for both CC values defined by two tenplates, and we did not show them in Table S1.

The result is summarized in Table S1, which is an extended version of Table 2 in the main manuscript.

3. Additional discussion for the performance of our method

Figure S5 summarizes the detection performance of three different *cf* stacks showing each of the *cf* values for detected events (true and false alarms). The vertical axis correlates roughly with the size of the events (catalog events are largest, events detected by visual inspection are next largest, etc.). The results with cf_{12} and cf_{123} show that the detectability of the events systematically correlates with the *cf* value; e.g., larger events have higher *cf* value. Stack cf_{123} shows the best relationship between *cf* value and empirical event size, which is a desired

response for a detector. Meanwhile, cf_{all} shows a range of values for the events detected by visual inspections, which means that cf_{all} values do not correlate well with event size. We infer that cf_{all} uses information from all boreholes and some of the information from more distant wells behaves like noise. From this evaluation of detector performance, cf_{123} is the best stack to use for event detection, as we mentioned in the Discussion part of the main manuscript.

List of Supplemental Figure Captions

Table S1. Complete table for comparing event detection using our method, STA/LTA, and template matching. Stacking methods for each method are described in the text. B1~6 are events detected by visual inspection, which we used as a benchmark to show that our method has detectability that is at least comparable to visual inspection. Low SNR1~7 are the low SNR events newly detected by our method that were not found by our initial visual inspection. Detection of these events means that a method performs better than visual inspection. FA is a false alarm. The 2nd column shows the rough rounded detected time for each detected event including false alarm. The last three rows summarize the detections made by the individual methods. As benchmarks, the detection results obtained using STA/LTA and template matching methods are also shown.

Figure S1. Evaluation of linearity (C_L) and DOA inclination (DOA_{inc}) on synthetic waveforms. (a) synthetic waveforms containing sinusoidal wave and uncorrelated band limited white noise. (b) C_L distribution in time and frequency. (c) C_L ($\overline{C_L}$) averaged over 5~15 Hz. (d) DOA_{inc} distribution in time and frequency. (e) DOA_{inc} ($\overline{DOA_{inc}}$) averaged over 5~15 Hz.

Figure S2. The shape of characteristic function to penalize the mismatch between measured *DOA* (DOA_{inc}) and reference DOA (DOA_0).

Figure S3. Example of waveforms of false alarm that is detected just after M1.9 event by our method when using cf_{all}, cf_{12}, and cf_{123}. The detection time is indicated in Figure 11 with a triangle marker immediately following the M1.9 event. Black lines are the onset of detection at the 4th level (200 m) sensor at station G67.

Figure S4. Example of waveforms of false alarm that is detected just after M2.2 event by our method when using cf_{all}, cf_{12}, and cf_{123}. The detection time is indicated in Figure 11 with a triangle marker immediately following the M2.2 event. Black lines are the onset of detection at the 4th level (200 m) sensor at station G67.

Figure S5. Detection performance with various characteristic functions. Detection results are shown as a function of the value of each *cf*. Vertical axis roughly correlates with event size. Colors of the dots indicate the different characteristic functions *cf*.

Table S1. Complete table for comparing event detection using our method, STA/LTA, and template matching. Stacking methods for each method are described in the text. B1~6 are events detected by visual inspection, which we used as a benchmark to show that our method has detectability that is at least comparable to visual inspection. Low SNR1~7 are the low SNR events newly detected by our method that were not found by our initial visual inspection. Detection of these events means that a method performs better than visual inspection. FA is a false alarm. The 2nd column shows the rough rounded detected time for each detected event including false alarm. The last three rows summarize the detections made by the individual methods. As benchmarks, the detection results obtained using STA/LTA and template matching methods are also shown.

		Our method			STA/LTA			Template matching		
Event	**Time from reference (sec)**	**Stack all: cf_{all} (0.2283)**	**Stack 1-2: cf_{12} (0.3204)**	**Stack 1-3: cf_{123} (0.3166)**	**Stack all: STA/LTA_{all} (0.2337)**	**Stack 1-2: STA/LTA_{12} (0.2821)**	**Stack 1-3: STA/LTA_{123} (0.2556)**	**Stack all: CC_{all}**	**Stack 1-2: CC_{12}**	**Stack 1-3: CC_{123}**
Catalog M1.9	749	detected	detected	detected	detected	detected	detected	detected	detected	Detected
FA	760	detected	detected	detected						
B2	763	detected	detected	detected				detected	detected	detected
B5	997	detected	detected	detected	detected	detected	detected	detected	detected	detected
Low SNR1	1144	detected	detected	detected						
B3	1958	detected	detected	detected	detected	detected	detected	detected	detected	detected
B6	2195	detected	detected	detected						
FA	2449		detected							
Low SNR2	2830		detected	detected					detected	detected
B4	3359	detected	detected	detected	detected	detected	detected		detected	detected
Catalog M2.2	3467	detected	detected	detected	detected	detected	detected	detected	detected	detected
FA	3481		detected							
FA	3483		detected	detected						
Low SNR3	3544	detected	detected	detected					detected	detected
Low SNR4	4106			detected						
FA	5883				detected		detected			
FA	5562		detected							

FA	6766	detected								
B1	7400	detected	detected	detected	detected	detected	detected	detected	detected	detected
FA	9543		detected							
FA	9901									
FA	10223		detected							
FA	10226									
Low SNR5	11243	detected	detected	detected					detected	detected
FA	11760		detected							
FA	11770		detected							
FA	11776		detected							
FA	11995		detected							
Low SNR6	12918	detected	detected	detected						
Low SNR7	13341		detected	detected						
Additional low SNR events		4	6	7	0	0	0	0	3	3
False alarms		2	11	2	1	0	1	0	0	0
Total		14	25	17	6	6	6	6	10	10

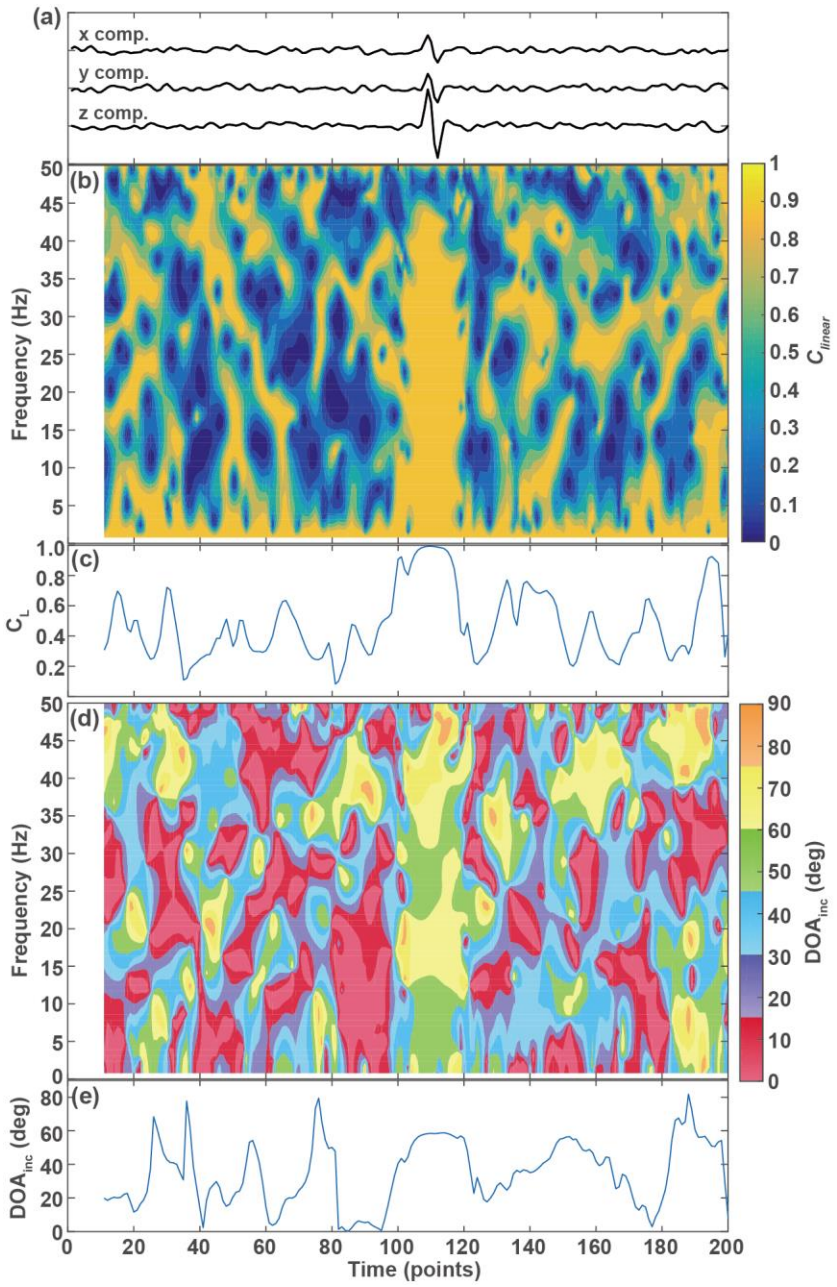

Figure S1. Evaluation of linearity (C_L) and DOA inclination (DOA_{inc}) on synthetic waveforms. (a) synthetic waveforms containing sinusoidal wave and uncorrelated band limited white noise. (b) C_L distribution in time and frequency. (c) C_L ($\overline{C_L}$) averaged over 5~15 Hz. (d) DOA_{inc} distribution in time and frequency. (e) DOA_{inc} ($\overline{DOA_{inc}}$) averaged over 5~15 Hz.

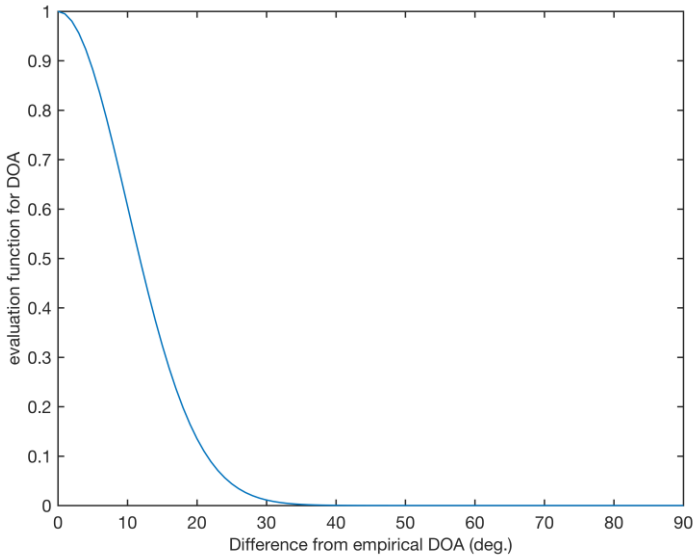

Figure S2. The shape of characteristic function to penalize the mismatch between measured *DOA* (DOA_{inc}) and reference DOA (DOA_0).

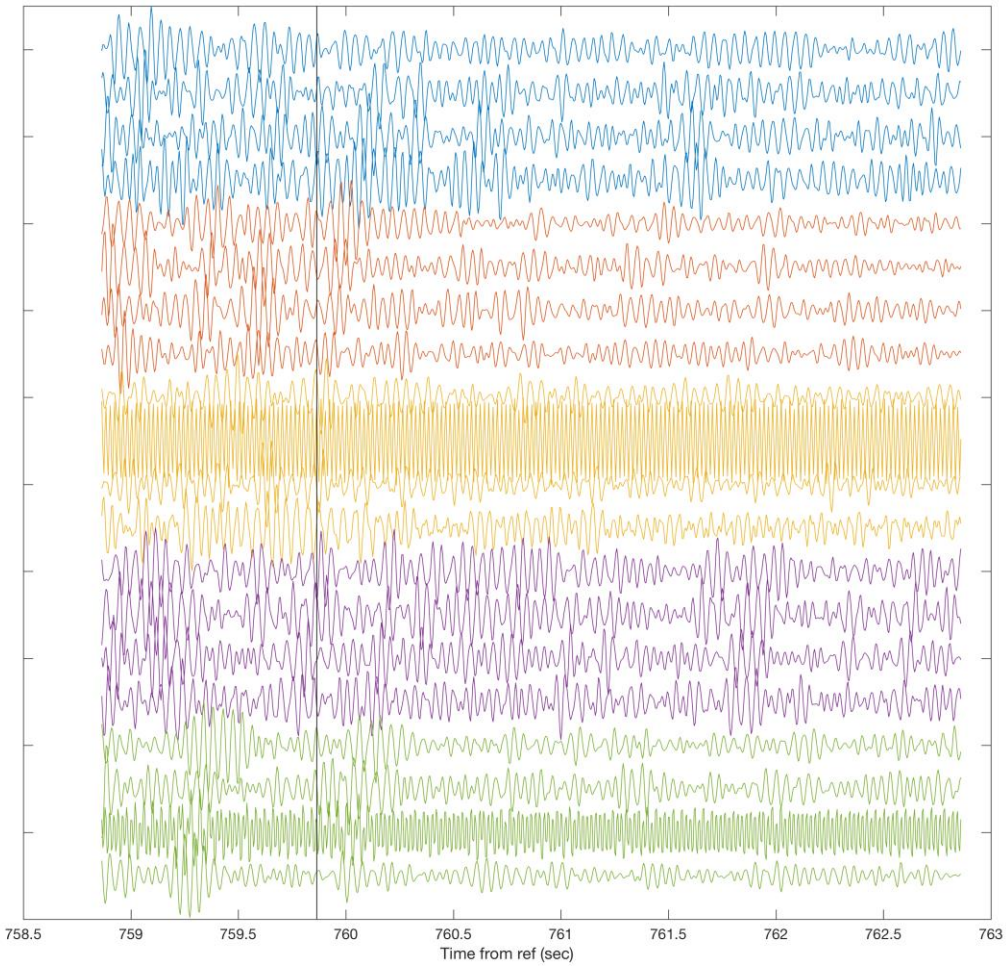

Figure S3. Example of waveforms of false alarm that is detected just after M1.9 event by our method when using cf_{all}, cf_{12}, and cf_{123}. The detection time is indicated in Figure 11 with a triangle marker immediately following the M1.9 event. Black lines are the onset of detection at the 4th level (200 m) sensor at station G67.

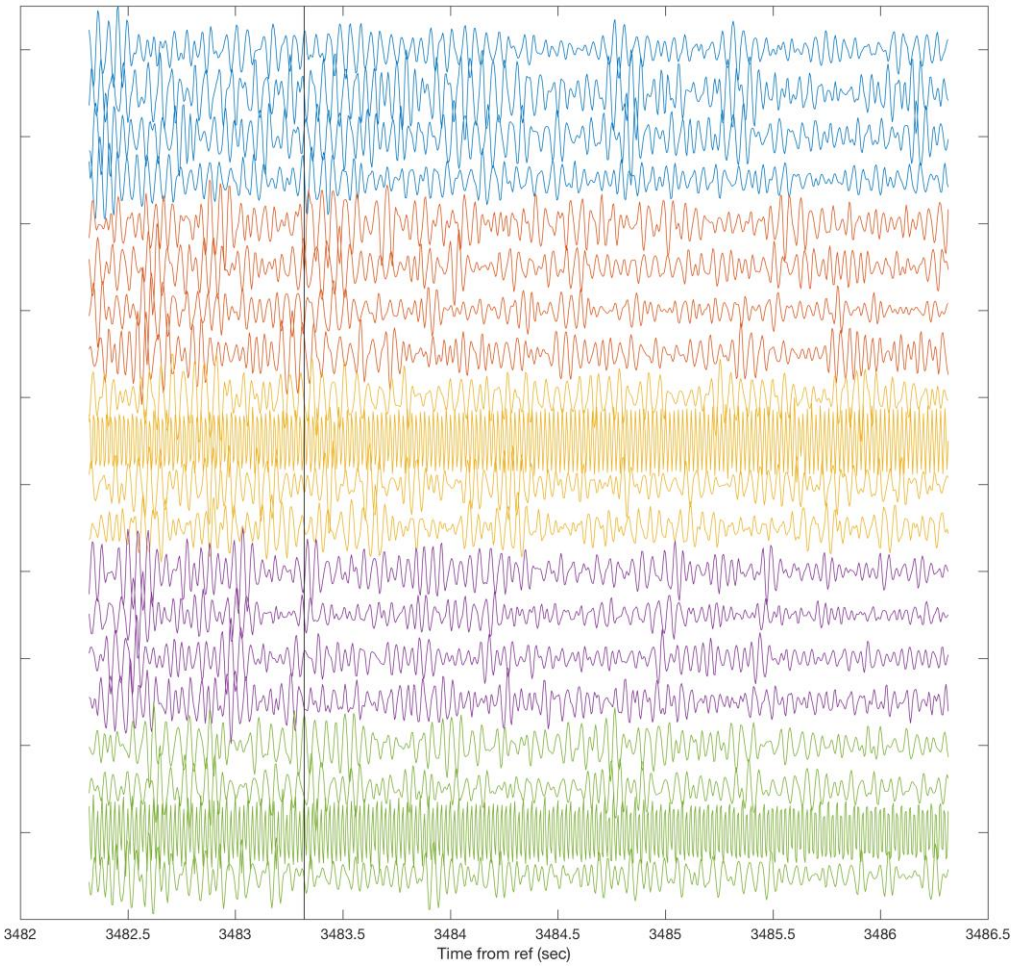

Figure S4. Example of waveforms of false alarm that is detected just after M2.2 event by our method when using cf_{all}, cf_{12}, and cf_{123}. The detection time is indicated in Figure 11 with a triangle marker immediately following the M2.2 event. Black lines are the onset of detection at the 4th level (200 m) sensor at station G67.

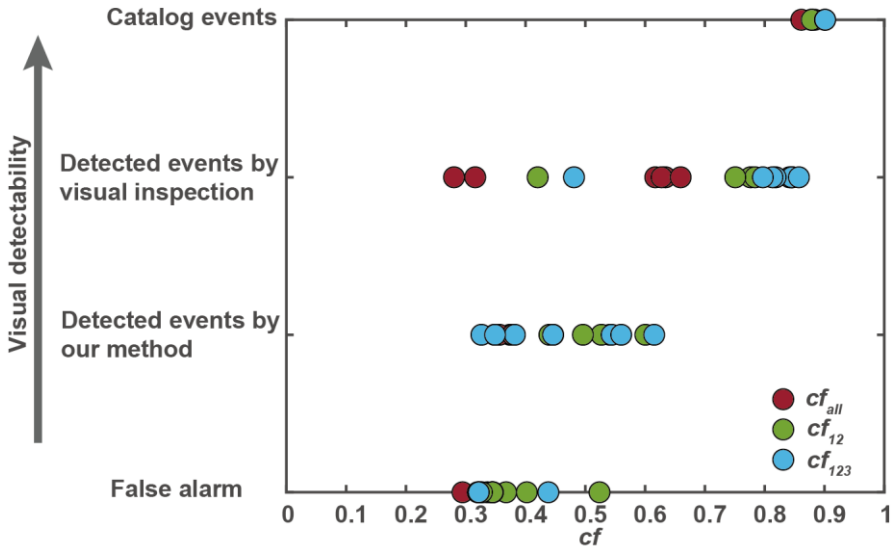

Figure S5. Detection performance with various characteristic functions. Detection results are shown as a function of the value of each *cf*. Vertical axis roughly correlates with event size. Colors of the dots indicate the different characteristic functions *cf*.